ChemPubSoc Europe

DOI: 10.1002/cssc.201402089

Nanostructured Tungsten Trioxide Thin Films Synthesized for Photoelectrocatalytic Water Oxidation: A review

Tao Zhu, Meng Nan Chong,* and Eng Seng Chan[a]

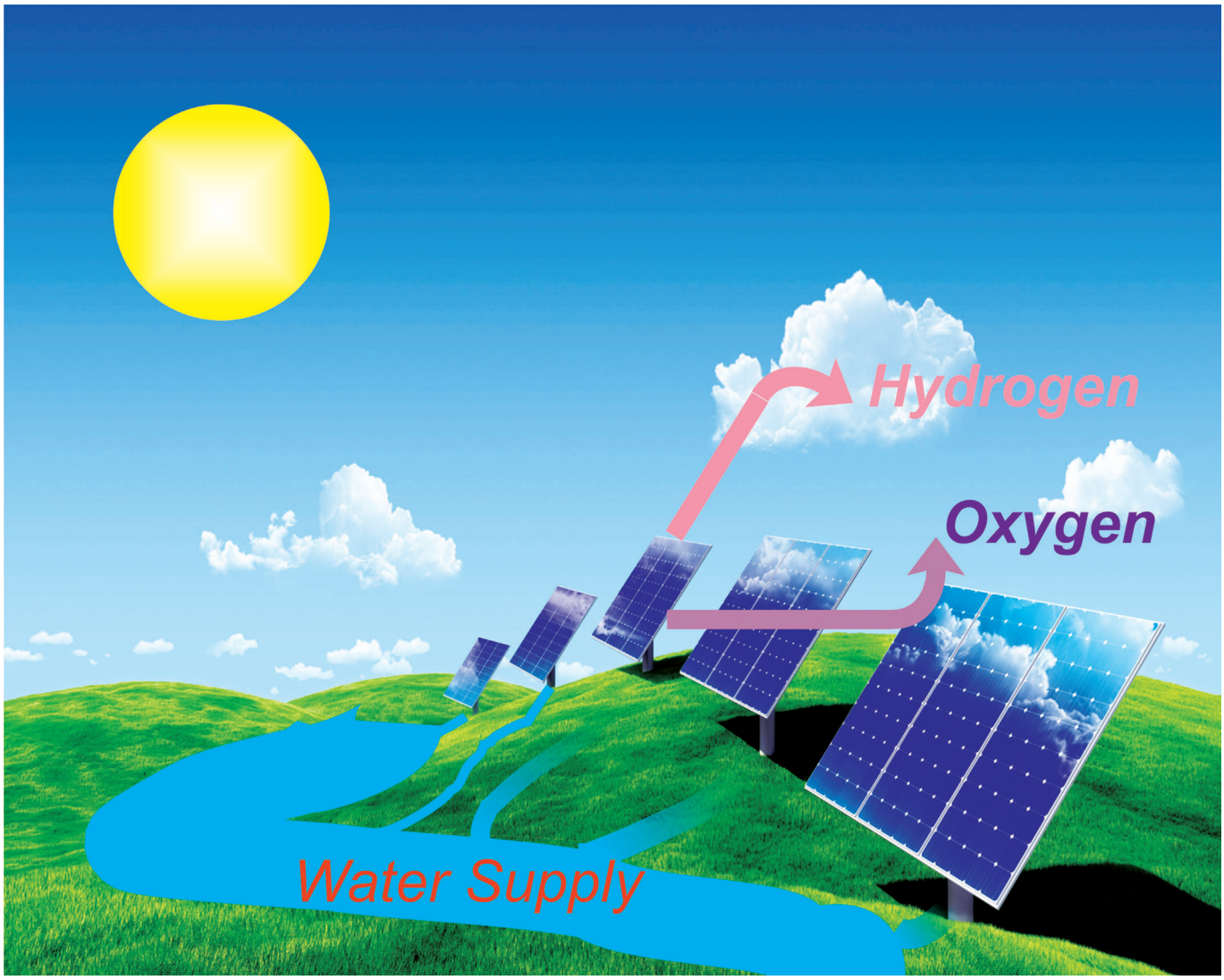

The recent developments of nanostructured WO_3 thin films synthesized through the electrochemical route of electrochemical anodization and cathodic electrodeposition for the application in photoelectrochemical (PEC) water splitting are reviewed. The key fundamental reaction mechanisms of electrochemical anodization and cathodic electrodeposition methods for synthesizing nanostructured WO_3 thin films are explained. In addition, the effects of metal oxide precursors, electrode substrates, applied potentials and current densities, and annealing temperatures on size, composition, and thickness of the electrochemically synthesized nanostructured WO_3 thin films are elucidated in detail. Finally, a summary is given for the general evaluation practices used to calculate the energy conversion efficiency of nanostructured WO_3 thin films and a recommendation is provided to standardize the presentation of research results in the field to allow for easy comparison of reported PEC efficiencies in the near future.

1. Introduction

Owing to the decline in fossil fuel supplies projected over the next decades, there is a serious devotion to the exploitation of renewable energy resources to resolve the potential future energy shortage. H_2 is a promising renewable energy resource, but 95% of the current H_2 production routes require the utilization of more costly carbon-based fuels for the synthesis, which makes it rather less cost effective and sustainable.[1] The production of H_2 through photoelectrochemical (PEC) water splitting has been reported by Fujishima and Honda in 1972[2] and has since been widely studied. In the PEC water splitting reaction, a water molecule is converted to H_2 and O_2 through the use of semiconducting metal oxide photocatalysts. Thus, photocatalysts play an important role in the water-to-hydrogen energy conversion process.

To date, various semiconducting metal oxide photocatalysts have been investigated and the feasible utilization of the solar spectrum for the photonic activation of photocatalysts depends on the band gap energy. The most common semiconducting metal oxide photocatalysts, such as ZnO,[3] Fe_2O_3,[4] and TiO_2,[3b,5] have been studied extensively. Among them, TiO_2 is the best known and most widely used semiconducting metal oxide photocatalyst. However, the band gap energy of TiO_2 is relatively high (3.2 eV) and, hence, it is only capable of absorbing 5–7% of the solar spectrum.[6] Unlike TiO_2, WO_3 has a considerably smaller band gap energy (2.6 eV) and is, therefore, capable of increased absorption in the visible light region (about 12% of the solar spectrum). Moreover, WO_3 exhibits a very high corrosion resistance in most acidic aqueous media.[7] To date, WO_3 has been reported in a number of studies as a new-generation photocatalyst for PEC water splitting.[8]

Various methods have been reported for fabricating semiconducting metal oxide photocatalysts with modified physical and chemical properties and improved photoactivity, such as sputtering methods,[8b,9] thermal evaporation,[9a,10] chemical vapor deposition,[11] cathodic electrodeposition,[12] electrochemical anodization,[13] and sol–gel[9a,14] and hydrothermal methods.[4b,15] Although it is well accepted that high-purity nanostructured WO_3 thin films can be obtained using almost all of the reported synthesis methods, most of them are not suitable to scale-up processing and for commercialization.[9a,10b] Recently, the electrochemical synthesis route has received considerable attention owing to the advantages of low cost, low processing temperature and pressure, direct control of film thickness, and the possibility of large-scale synthesis.[16]

Herein, we review electrochemical synthesis routes for the synthesis of nanostructured WO_3 thin films. First, we discuss the key fundamental reaction mechanisms of electrochemical anodization and cathodic electrodeposition. This is followed by a critical review and discussion of the effects of metal oxide precursors, electrode substrates, applied potentials and current densities, and annealing temperatures on the size, composition, and thickness of the nanostructured WO_3 thin films. Finally, general evaluation practices to calculate energy conversion efficiencies of nanostructured WO_3 thin films are summarized and a recommendation is provided to standardize the research results reported to allow for easy comparison of PEC efficiencies in the near future.

2. Electrochemical Synthesis of Nanostructured WO_3

The electrochemical route is probably the most cost-effective synthesis method, as it does not require expensive instrumentation to synthesize stoichiometric nanostructured WO_3 thin films in addition to forming films with large surface area-to-volume ratios.[17] The electrochemical route is usually performed either through electrochemical anodization or cathodic electrodeposition. These electrochemical synthesis methods offer a versatile and approach room temperature to produce advanced nanostructured WO_3 thin films, such as epitaxial,[18] superlattice,[19] quantum dot,[20] and nanoporous[21] films. By varying the electrochemical synthesis parameters, such as metal oxide precursor, electrode substrate, applied potential and current density, and annealing temperature the nanostructured WO_3 thin films can be tailored to exhibit desirable physical and chemical properties.[22]

2.1. Electrochemical anodization

Electrochemical anodization is a versatile method to synthesize nanostructured WO_3 thin films because it produces the most ordered nanoporous structures and yet offers a simple, effi-

[a] T. Zhu, Dr. M. N. Chong, Prof. E. S. Chan
Advanced Engineering Platform and School of Engineering
Monash University Malaysia
Jalan Lagoon Selatan, Bandar Sunway
Selangor Darul Ehsan, 46150 (Malaysia)
E-mail: chong.meng.nan@monash.edu

cient, and cost-effective method to control the growth of a thin film over a large surface area.[22b] Anodization of metals is a well-established technique for the synthesis of metal oxide structures on metal electrodes. Anodization is carried out by applying potentials and/or current densities in a PEC cell setup (Figure 1), where the metal is used as the anode. Equations (1) and (2) show the half reactions that occur in a PEC cell setup at both the anode and cathode.

$$\text{Anode}: \ M + H_2O \rightarrow MO_x + H^+ + e^- \quad (1)$$

$$\text{Cathode}: \ H_2O \rightarrow OH^- + H_2 + 2e^- \quad (2)$$

Tao Zhu received his Bachelor degree from the College of Resources and Environment Engineering, Wuhan University of Technology. Thereafter, he also pursued a Masters degree in Chemical Engineering from Huazhong University of Science and Technology. Currently, he is pursuing his PhD degree under the supervision of Dr. Meng Nan Chong and Prof. Eng Seng Chan at Monash University Malaysia. His research interests mainly focus on the electrochemical synthesis and improvement of photocatalyst tungsten trioxide (WO_3) for water splitting.

Meng Nan Chong is a Senior Lecturer at Monash University Malaysia. He is also the principal investigator for this research project funded by Ministry of Science, Technology and Innovation (MOSTI), Malaysia. He received his first class honors Bachelor degree in Chemical Engineering and a PhD in Engineering, both from the University of Adelaide. Prior to Monash University, he worked as a Research Engineer and Project Leader at Commonwealth Scientific and Industrial Research Organisation (CSIRO), Australia. His research interests are synthesis and application of photocatalysts for environmental remediation as well as integrated water resource management.

Eng Seng Chan received his B. Eng. and PhD from the Department of Chemical Engineering, University of Birmingham, UK. He is an Associate Professor at the School of Engineering, Monash University Malaysia, where he presently heads the Chemical Engineering Discipline. His current research involves structuration of materials for energy production, water purification, and drug delivery.

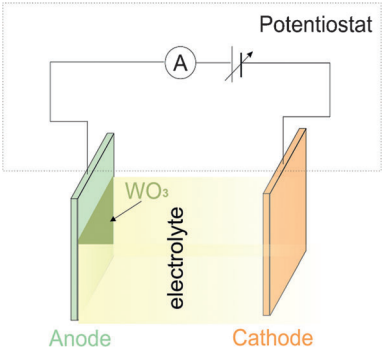

Figure 1. Electrochemical anodization method for synthesizing nanostructured WO_3 thin films. Generally, anode and cathode are W foil and Pt, respectively.

where M represents the metal used in the electrochemical anodization. Equation (1) represents the growth of the WO_3 layer, whereas H_2 evolution occurs at the cathode according to Equation (2). A considerable amount of fundamental research has been performed to investigate in detail the mechanistic aspects of the electrochemical growth of WO_3 in aqueous media. Based on electrochemical and XPS data, it has been proposed that the initial anodic oxidation of W may result in the formation of a mixture of oxides, namely WO_2, W_2O_5, and WO_3, as depicted in [Eqs. (3)–(5)]. However, it was reported that the dominating species at higher anodization potentials (>2 V) is W^{6+}.[13b]

$$W + 2H_2O \rightarrow WO_2 + 4H^+ + 4e^- \quad (3)$$

$$2WO_2 + H_2O \rightarrow W_2O_5 + 2H^+ + 2e^- \quad (4)$$

$$W_2O_5 + H_2O \rightarrow 2WO_3 + 2H^+ + 2e^- \quad (5)$$

Table 1 summarizes the various electrochemical approaches for the synthesis of nanostructured WO_3 thin films through anodization: even when using the electrochemical anodization method alone, different synthesis approaches can be adopted as evidenced by the various pretreatments, electrolytes, applied potentials, and annealing temperatures used. The differences in the electrochemical synthesis parameters yield nanostructured WO_3 thin films with different physical and chemical properties such as particle size, surface uniformity, pore diameter, structure length, film thickness, and photoactivity. For instance, Fraga et al. prepared W/WO_3 thin films by anodization of W foil in a NaF solution by using a conventional two-electrode electrochemical cell.[23] They found that the particle size of the nanoporous WO_3 layer formed was around 100 nm and that the thin film had a great uniformity. Moreover, the absorption of the thin films was extended to wavelengths above 480 nm (into the visible light spectrum) and thus, good photoactivity is achieved.[23] Hahn et al. reported the use of a three-electrode electrochemical cell to prepare WO_3 in an electrolyte containing $HClO_4$ and $NaClO_4$ applying a potentials in the ranges from 10–100 V.[24] They concluded that the nanoporous WO_3 structure formed had a uniform surface with an average pore diameter of 40 nm and a pore length of 16 μm.[24] The

Table 1. Summary of various electrochemical synthesis approaches of WO_3 thin films via anodization method.

Ref.	Pretreatments	Electrolyte	Applied potential/ current	Annealing temperature	Morphology	Photocurrent
[23]	polishing of W foil using SiC sandpaper and washing with acetone, isopropanol, , water, then dried with N_2	0.15 м NaF	60 V (two-electrode configuration) with ramp potential of 0.2 V s^{-1}	450 °C 30 min	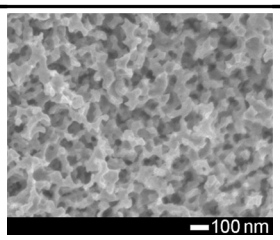	17 mA cm^{-2} at 1.5 V (vs. Ag/AgCl, KCl saturated) in 0.1 м Na_2SO_4 (pH 2.0) under 150 W Xe lamps
[24]	degreasing of Ti and W foils by sonication in acetone, isopropanol, and methanol; followed by rinsing with deionized water and drying in N_2 stream; the samples were pressed together using a Cu-plate contact against an O-ring	$HClO_4$, $NaClO_4$ (0.01, 0.05, 0.1, and 1 м)	10–100 V (vs. Ag/AgCl 1 м KCl)	–	–	–
[22b]	–	10 wt% K_2HPO_4 and glycerol 95 °C	50 V (two-electrode configuration) with or without exposure to light source	400 °C 5 h	–	2 mA cm^{-2} at 2.0 V (vs. Ag/AgCl 3 м KCl) in 0.33 м H_3PO_4 under 100 mW cm^{-2}
[25]	cleaning of W foils by immersion in an acetone ultrasonic bath for 10 min, followed by rinsing with deionized water and drying in air	0.25 м oxalic acid	galvanostatic at room temperature	350 °C in oxygen atmosphere 3 h	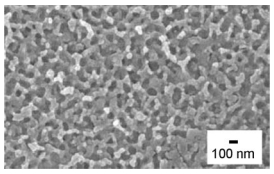	–
[26]	sonicating W sheets in acetone, isopropanol, and methanol successively; followed by rinsing with deionized water and drying in a N_2 stream	1 м H_2SO_4 and 0.5 wt% NaF	40 V (vs. Ag/AgCl 1 м KCl) with a potential ramp 1000 mV s^{-1}	450 °C for 1 h in ambient air	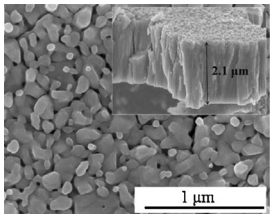	14 μA cm^{-2} at 1 V (vs. Ag/AgCl) in 0.33 м H_3PO_4 under oriel 6356 Xe lamp
[28]	degreasing of W foil by sonication in acetone, isopropanol, and methanol successively; followed by rinsing in deionized water and drying in N_2 stream	different concentrated NaF solution	20, 40, and 60 V (Ag/AgCl 1 м KCl) with different period	–	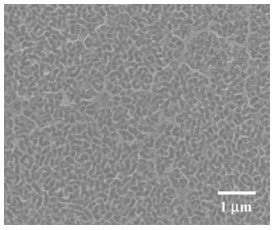	–
[9c]	RF sputtering of W thin films on FTO glass	NH_4F 0.5 wt%/ethylene glycol	constant 100 W RF power	450 °C in 90% O_2 for 4 h	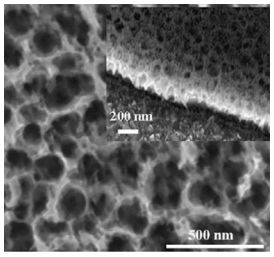	40 μA cm^{-2} with no biased voltage in 0.1 м Na_2SO_4 under UV/Vis illumination
[8c]	mechanical polishing of W foils using SiC sandpaper; followed by anodization in an alkaline electrolyte at a low voltage to remove the oxide layer	1 м Na_2SO_4 and 0.5 wt% NaF	20, 40, and 60 V (two-electrode configuration) for 2 h	723 K in an oxygen atmosphere for 3 h	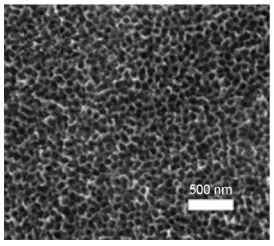	0.5 mA cm^{-2} at 1.5 V (saturated Ag/AgCl) in 0.5 м Na_2SO_4 under 100 mW cm^{-2} Xe lamp

Table 1. (Continued)

Ref.	Pretreatments	Electrolyte	Applied potential/ current	Annealing temperature	Morphology	Photocurrent
[13b]	sonicating W foils in an aqueous alcohol solution for 10 min; followed by rinsing with water and washing with ethanol and acetone	NMF/H_2O 8:2 and 0.05% *w/w* NH_4F	40 V (two-electrode configuration) with increased rate at 0.5 V s^{-1}	550 °C in air for 1 h	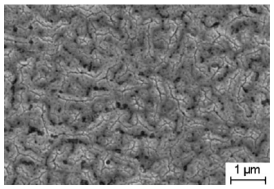	9 mA cm^{-2} at 1.7 V (SCE) in 1 M H_2SO_4/ CH_3OH 8:2 under 0.120 W cm^{-2}
[27]	cleaning of W foils in four 15 min steps in acetone, isopropanol, methanol, and finally deionized water; followed by drying in N_2 stream	$NH_4/(NH_4)_2SO_4$	50 V (two-electrode configuration) for 30 min	300–650 °C in pure N_2	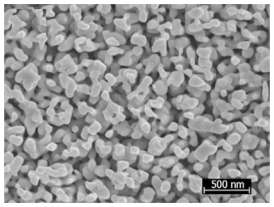	3.0 μA cm^{-2} at 1.2 V in 0.5 M H_2SO_4 (pH 0) under 100 mW cm^{-2} Xe lamp

morphology of the oxidized metal surface can be controlled by using a new electrochemical anodization under visible light. Kim et al. used the PEC anodization method for the preparation of a thick WO_3 film and achieved a significantly higher photoactivity at a film thickness of 2.6 μm.[22b] In this case, the thickness of the WO_3 film was double that of the WO_3 film prepared using a conventional electrochemical anodization method. The increased WO_3 film thickness produced using the PEC anodization method was partly attributed to either the higher degree of formation of crystalline outer oxide layers or the acceleration of pore-wall dissolution at the tip of the pores due to holes generated by illumination.[22b] Mukherjee et al.[25] applied a constant current density for the anodization of W in oxalic acid as electrolyte and synthesized a highly regular nanoporous WO_3 structure. The nanoporous WO_3 structure had a smaller pore size range of 50–100 nm than that reported from most sol–gel synthesis methods of W in 0.25 M oxalic acid electrolyte.[25]

Nah et al.[26] reported the growth of nanoporous WO_3 layers through anodization of W in a F^--containing electrolyte, which was later exposed to thermal treatment in NH_3 for nitrogen doping. The nitrogen-doped WO_3 layers exhibited photocurrents; these were significantly improved by increased absorption in the visible light region. Liu and co-workers found that nitrogen can be doped successfully into nanoporous WO_3 photoelectrodes by controlling the annealing temperature.[27] Tsuchiya et al. investigated the preparation of WO_3 in electrolytes containing different concentrations of NaF in a three-electrode electrochemical system.[28] They found that the pores of the self-organized porous WO_3 layers were very regular and had an average pore diameter of 100 nm. Zheng et al.[9c] reported the electrochemical anodization of radio-frequency (RF) sputtered W thin films on fluorine-doped tin oxide (FTO) glass that resulted in a uniformly structured porous WO_3 films. Zhang et al.,[8c] fabricated the nanoporous WO_3 by anodizing W foil. They obtained nanoporous WO_3 with an average pore size of about 80 nm and found that this WO_3 nanoporous structure had a better photoactivity under visible light in comparison to a planar structure.[8c] Cristino et al.,[13b] prepared WO_3 thin films obtained through method in a two-electrode electrochemical cell configuration. They concluded that the anodization leads to highly efficient WO_3 photoanodes owing to absorption of higher wide visible spectral and electrochemical active surface and improved charge-transfer kinetics under simulated solar illumination.[13b]

2.2. Cathodic electrodeposition

Similarly, cathodic electrodeposition also allows the precise control of the thickness of the nanostructured WO_3 film, which is useful for a cost-effective scale-up of processing. The cathodic electrodeposition method is shown in Figure 2, and the various methods are summarized in Table 2. Other advantages of cathodic electrodeposition include its potential for mass production as well as the ability to produce nanostructured WO_3 thin films with large surface area-to-volume ratios.[29] There are two different mechanisms for the cathodic electrodeposition method, which are (1) the direct reduction of the oxidation state of metals and its deposition on the electrodes and (2) an increase in the interfacial pH value and local supersaturation followed by metal oxide precipitation.[12b] The latter mechanism is usually based on the generation of a localized high-

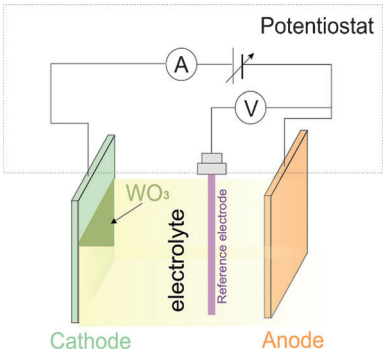

Figure 2. Cathodic electrodeposition method for synthesizing WO_3 thin films, where the cathode usually uses FTO or ITO as electrode substrate whereas Pt is employed as the anode.

Table 2. Summary of various electrochemical synthesis approaches of WO_3 thin films via cathodic method.

Ref.	Precursor preparation	Substrate	Applied potential/current/time	Annealing temperature/time	Morphologies	Photocurrent
[37]	W dissolved in H_2O_2 (20%)	Pt foil	3.0 V (vs. SCE)/–/–	$>100\,^{\circ}C$/1 h	–	–
[38]	Na_2WO_4 and H_2O_2 at controlled pH 1.2 (adjusted by H_2SO_4) to yield a ratio $[H_2WO_4]/[H_2O_2]=1:0.03$.	ITO-coated glass	–/1.0 mA cm^2 peak current density/pulsed square waves with both "on" and "off" time of 4.0 ms	100–400 °C/60 min	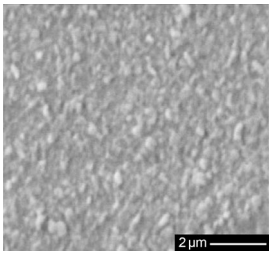	–
[39]	W powder (2 g, 99% purity) dissolved in H_2O_2 (30%; pH 2 adjusted by H_2SO_4); bath temperature 300 K, concentration 0.1 N	SnO_2-coated plate	–/0.5 mA (galvanostatic)/deposition 90 min	–	–	–
[17]	W (2 g) powder dissolved in H_2O_2 (20%) and addition of a few drops of H_2SO_4	conducting transparent oxide (CTO)-coated glass (10 Ω/□ sheet resistance)	–/0.5, 0.65, and 0.75 mA cm^2 (galvanostatic)/30–120 min	–	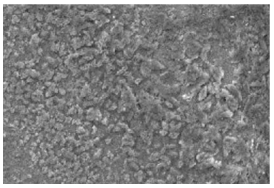	–
[40]	Na_2WO_4 dissolved in H_2O_2 (30%; pH adjusted to 1.2 by $HClO_4$); concentration ratio H_2O_2/WO_4^{2-} ranging from 0 to 4	F:SnO-coated glass (Nippon Sheet Glass (NSG), 10 Ω/□) and quartz oscillators	0.06 to −0.34 V vs. NHE (under Ar)/–/–	–	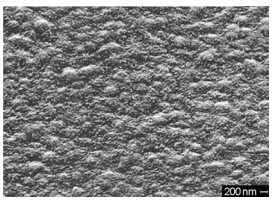	–
[41]	H_2PtCl_6 (0.001 M) and Na_2WO_4 (0.01 M) dissolved in 0.5 M H_2SO_4	commercial gas diffusion layer (microporous carbon on carbon cloth)	various ranges at RT (24±2 °C) under continuous bubbling of N_2 to eliminate O_2	–	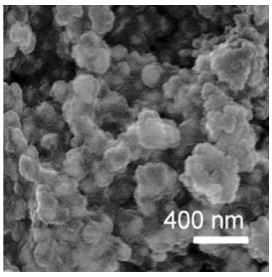	–
[33]	W powder (6.5 g) dissolved in H_2O_2 (30%, 40 mL) and distilled water (4 mL) at 5 °C (adjusted using a chilled water bath while stirring continuously); the W peroxide solution was stored in the refrigerator for ~7 days at 2 °C	SnO2:F-coated glass sheet (trade name: K-glass)	<-450 mV/1–2 mA cm^2/10 min	–	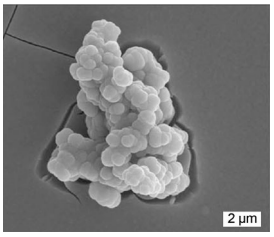	–
[34]	Na_2WO_4 (25 mM) and H_2O_2 (0.075%, pH adjusted to 1.4 by HNO_3)	FTO-coated glass as substrate with ~400 nm thick and 10.3 Ω/□	−0.45 V (vs. Ag/AgCl in satd. KCl)/–/25 min	350 °C/30 min	–	0.35 mA cm^{-2} at 1.2 V (vs. Ag/AgCl in satd. KCl) in 0.1 M Na_2SO_4 under 75 W Xe lamp
[42]	W powder (1.8 g) dissolved in H_2O_2 (30%, 60 mL); followed by decomposition of excess peroxide using Pt black and dilution of the solution to 50 mM using a water/isopropanol (50:50) mixture or sodium dodecyl sulfate (SDS) solution	ITO-coated glass	−0.2 to −0.5 V (vs. Ag/AgCl in 4 M KCl)	–	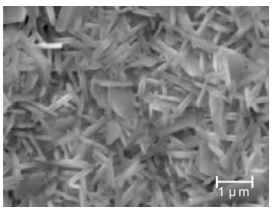	20 µA cm^{-2} without biased voltage in 0.1 M CH_3OONa under 150 W Xe lamp (25 mW cm^{-2})

Table 2. (Continued)

Ref.	Precursor preparation	Substrate	Applied potential/current/time	Annealing temperature/time	Morphologies	Photocurrent
[43]	carboxylic acid (0.03 M; formic, oxalic, or citric acid) and W (0.2 M)	FTO-coated glass	−0.4 V (vs. Ag/AgCl)/–/15–60 min	450 °C (in air after cleaning)/2 h	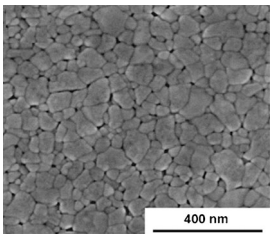	0.14 mA cm^{-2} at 0.7 V (vs. Ag/AgCl) in 0.1 M Na_2SO_4/under tungsten–halogen lamp 100 mW cm^{-2}
[12a]	W foil dissolved in H_2O_2 (30% *w/w*) replaced W powder for electrodeposition solution; resulting solution diluted through addition of propan-2-ol to obtain various W concentrations (0.05, 0.1, and 0.2 mol dm^{-3} at pH 2.14, 1.18 ,and 1.68, respectively)	FTO-coated glass (15 Ω/□; 3.0 cm × 2.5 cm)	−0.4 V (vs. Ag/AgCl)/–/120 min at 30 min increments	450 °C (in air)/2 h	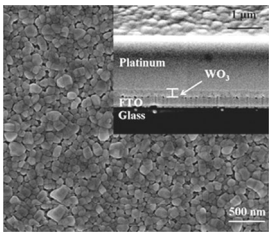	0.08 mA cm^{-2} at 0.9 V (vs. Ag/AgCl) in 0.5 M NaCl under tungsten–halogen lamp 100 mW cm^{-2}
[30]	W powder (4.6 g) dissolved in H_2O_2 (30% *w/w*, 25 mL); solution diluted to 50 mM W using water/isopropanol (70:30 *v/v* at pH 1.9)	Sn-doped ITO-coated glass with 30 or 100 Ω/□ (100 and 35 nm thickness, respectively)	−0.5 V (vs. Ag/AgCl)/–/–	–	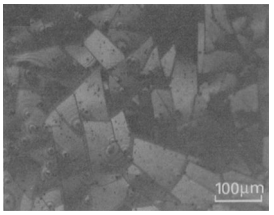	–
[44]	W (1.8 g) dissolved in H_2O_2 (30%, 60 mL); excess of H_2O_2 decomposed by Pt flakes before dilution to 50 mM using a 1:1 water/SDS solution (5 wt%)	modified graphite electrode	−0.5 V (vs. SCE) at 50 °C/–/–	–	–	–
[29]	W powder (1.8 g) dissolved in H_2O_2 (30%, 50 mL) for 24 h; excess of H_2O_2 decomposed by Pt black; dilution of solution to 50 mM by addition of water/2-propanol (~150 mL, 50:50 *v/v*) at pH 1.92 (adjusted by addition of H_2SO_4)	ITO-coated glass	–	up to 450 °C (in air; three-electrode setup)/10 min	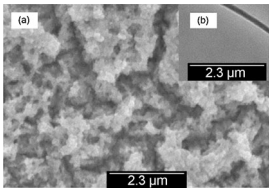	0.018 mA cm^{-2} at 0.9 V (vs. Ag/AgCl) in 0.1 M H_2SO_4 under 150 W EKE lamp
[16]	Na_2WO_4 (0.013 M) dissolved in H_2O_2 (0.03 M) and HNO_3 (0.05 M) at RT (pH 1.4)	Ti	–/5 mA cm^{-2} (galvanostatic)/30 min	–	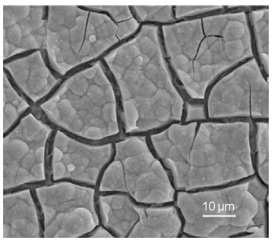	–
[45]	Na_2WO_4 (0.35 g) dissolved in distilled water (10 mL) and H_2O_2 (0.1 mL) at pH 1–2 (adjusted by HNO_3)	ITO-coated glass	−0.65 V (vs. Ag/AgCl in satd. KCl)/10 min	–	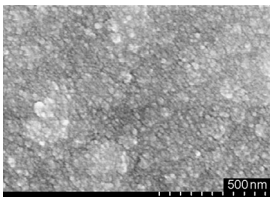	–
[32]	H_2WO_4 (0.15 M) dissolved in H_2SO_4 (0.5 M) and H_2O_2 (0.08 M)	carbon cloth (geometric area 0.78 cm^2)	deposition through 25 cyclic voltammetric scans from −0.6 to 0.9 V (vs. SCE)	–	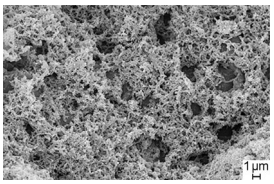	–

Table 2. (Continued)

Ref.	Precursor preparation	Substrate	Applied potential/current/time	Annealing temperature/time	Morphologies	Photocurrent
[46]	W powder dissolved in excess H_2O_2 to yield peroxo-tungstic acid (0.1 M); addition of high purity water and isopropyl alcohol/ethylene glycol while stirring; resulting pH value of ~1.3	FTO (8–12 Ω/□)	−600 mV (vs. Ag/AgCl)	500 °C (in air)/1 h	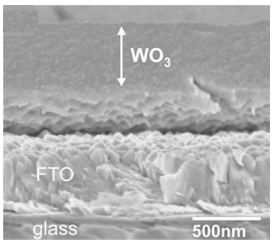	1.4 mA cm^{-2} at 1.0 V (vs. Ag/AgCl) in 0.1 M CH_3COONa under 400 mW cm^{-2} with an AM 1.5G filter
[47]	W powder (1 g) dissolved in H_2O_2 (30% *w/w*, 4 mL) at pH 1.35 (adjusted by HCl); solution was stirred for 24 h at RT	ITO-coated glass	−0.6 V vs NHE	–	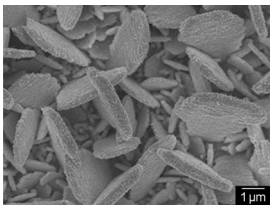	0.8 mA cm^{-2} at 1.4 V (vs. NHE) in 0.5 M H_2SO_4 under 0.1 W cm^{-2} Xe light irradiation
[48]	Na_2WO_4 (25 mM) and H_2O_2 (0.075%) at pH 1.4; precursor for TiO_2: Ti powder dissolved in a solution containing H_2O_2 and NH_3 at pH 1.7	FTO coated on soda–lime glass	WO_3/TiO_2 films prepared by switching baths for 5 cycles at −0.45 (for WO_3) and −0.95 V (for TiO_2) (vs. Ag/AgCl satd. KCl)	450 °C/30 min	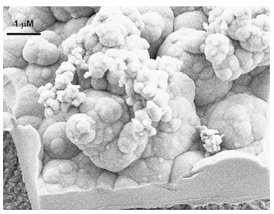	1.4 mA cm^{-2} at 1.2 V (vs. Ag/AgCl in satd. KCl) in 0.5 M Na_2SO_4 under 2.2 mW cm^{-2} Xe arc lamp (75 W)
[35]	colloidal triad solution containing peroxotungstic acid (25 mM), $[Ru(bpy)_3]^{2+}$ (1 mM), and PSS (30 mM)	ITO-coated glass	−0.45 V (vs. Ag/AgCl)	–	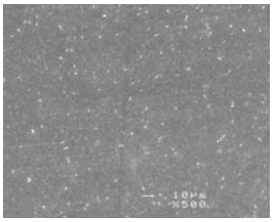	–

pH region near the electrode surface, which induces the electrodeposition of metal ions. The mechanisms of electrodeposition of WO_3 can be described by two reaction steps [Eqs. (6) and (7)]:[30]

$$2\,W + 10\,H_2O_2 \rightarrow W_2O_{11}{}^{2-} + 2\,H^+ + 9\,H_2O \quad (6)$$

$$W_2O_{11}{}^{2-} + (2+x)\,H^+ + x\,e^- \rightarrow 2\,WO_3 + (2+x)/2\,H_2O + (8-x)/4\,O_2 \quad (7)$$

where $W_2O_{11}{}^{2-}$ corresponds to $[(O_2)_2W(O)OW(O)(O_2)_2]^{2-}$and (O_2) denotes a peroxide ligand.[12a]

Meulenkamp proposed that the increase in efficiency of nanostructured WO_3 thin films was determined only to a good approximation by the reduction of peroxy tungstate.[30] However, the proposed mechanism strongly contradicted that of many other metal oxides, which are usually based on the two generalized mechanisms for cathodic electrodeposition discussed above. In general, the nanostructured WO_3 thin films can be cathodically electrodeposited from a solution containing dissolved W.[31] During the preparation of the precursor solution, most researchers will decompose the excess of H_2O_2 used for the preparation completely by using Pt black. Contrary to that, Zou et al.,[32] used cyclic voltammetry (CV) to deposit pure WO_3 films and found that the addition of a small volume of H_2O_2 to the precursor solution facilitated the deposition of WO_3. This method led to an enhanced energy storage capacity of the composite films, especially in the negative potential range.[32] Apart from these advantages, cathodic electrodeposition also permits the exact control of film thickness (unlike, e.g., spin-coating) and is suitable for the fabrication of composite films that incorporate two or more compounds, such as WO_3–CeO_2, WO_3–TiO_2, and others.[33] For instance, Yang et al. synthesized WO_3 films on indium-doped tin oxide (ITO) glass by performing the continuous cathodic electrodeposition method.[29] They found that the morphology of WO_3 films can be controlled by varying the H_2SO_4 concentration in the electrolyte. Vijayalakshmi and co-workers studied the effect of different deposition current densities on the physical and chemical properties of WO_3 thin films.[17] At a current density of 0.5 mA cm^{-2}, they found that the surface showed no pinholes in scanning electron microscopy (SEM) images. Tacconi et al.[34] synthesized semiconducting WO_3–TiO_2 composite films by using a novel approach in cathodic electrodeposition. The pre-

cursor solution was prepared by using 25 mM Na_2WO_4 and 0.075% H_2O_2 at pH 1.4 whereas the precursor solution for TiO_2 was prepared by dissolving Ti powder in a solution containing H_2O_2 and NH_3 at pH 1.7. They found that the composite films contained comparable amounts of WO_3 and TiO_2, which showed superior PEC performance in 0.1 M Na_2SO_4 relative to the pure metal oxides.[34] Yagi et al.[35] fabricated a hybrid WO_3/$[Ru(bpy)_3]^{2+}$/PSS (bpy = tris(2,2′-bipyrizine) PSS = poly(sodium 4-styrensufonate)) film by electrodeposition from a colloidal triad solution containing 25 mM peroxotungstic acid, 1 mM $[Ru(bpy)_3]^{2+}$, and 30 mM PSS at a potential of −0.45 V (vs. Ag/AgCl). They found that the film thickness was constant (0.62 ± 0.026 μm) and that the maximum absorption was at λ_{max} = 459 nm. Zhao et al.[36] investigated the WO_3/Ag–Bi photocatalyst and found that the photocatalyst showed excellent catalytic activity for water splitting. The WO_3/Ag–Bi photocatalyst showed a high O_2 evolution rate of 30.85 μmol h^{-1}, a high faradaic efficiency of 91.3%, and a low O_2 evolution overpotential of 290 mV.

Organic and inorganic nanocomposite films have also been widely studied. Wei et al.[16] synthesized WO_3/p-Cu_2O(p=positive type) and WO_3/n-Cu_2O(n=negative type) composite films with consecutive cathodic electrodeposition on Ti substrates. They found that the WO_3/p-Cu_2O exhibited a higher photoactivity compared to the activities of WO_3 and p-Cu_2O. They also found that the photoactivity of WO_3/n-Cu_2O was higher than that of pure WO_3 but lower than that of n-Cu_2O alone.[16] Yin et al. employed the cathodic electrodeposition method to produce WO_3/poly-3-methoxythiophene (PMOT) films on ITO-coated glass.[45] Their results showed that the WO_3/PMOT nanocomposite films consisted of two distinct layers: (1) substrate WO_3 layer with 30 nm grain size and (2) superstratum PMOT layer with an average grain size of 60 nm.

Most often, the low-cost material WO_3 nanocomposite thin films formed using the cathodic electrodeposition method are limited by their relatively high electrical resistivity.[49] However, this problem can be resolved by doping foreign elements into the lattice structure of WO_3. Martín et al. prepared electrodeposited Pt–WO_3 films from a fresh solutions 0.011 M H_2PtCl_6, 0.01 M Na_2WO_4 in 0.5 M H_2SO_4 by using a commercial gas diffusion electrode (e.g., microporous carbon on carbon cloth) as working electrode.[41] They concluded that a decrease in the electroactive area of Pt will increase the internal resistance of the cell, which will eventually lead to a reduction in the PEC water splitting efficiency.

Monk and Chester prepared the cathodic electrodeposition solution by dissolving W powder in H_2O_2 solution.[37] Their results showed that the diffusion coefficients of intercalating ions do not vary greatly with film composition. They also concluded that the charge transfer resistances are dramatically affected by the film composition. Contrarily, Yu et al. argued that the cathodic electrodeposition synthesis method was very difficult and time-consuming as the synthesized thin films were slightly gelatinous and fragile.[38] Pauporte developed a simple and fast method for preparing the cathodic electrodeposition solution by dissolving Na_2WO_4 in high-purity water and by adding 30% H_2O_2 in a conventional three-electrode electrochemical cell.[40] The WO_3 thin films formed were found to be amorphous, well surface covering, and dense up to 10 nm while also exhibiting an increased porosity at higher film thicknesses.

In addition, there are also other novel electrodeposition approaches reported in the literature. Leftheriotis and Yianoulis prepared the cathodic electrodeposition solution by storing the tungsten peroxide solution in a refrigerator for about seven days at 2 °C.[33] They obtained WO_3 films with modified morphologies of 1300 nm thickness. They also concluded that WO_3 films synthesized after 48 h of precursor preparation results in a higher effective surface area. Baeck et al. proposed a novel electrochemical synthesis approach for the synthesis of nanostructured WO_3 thin films whereby they obtained mesoporous WO_3 films with lamellar structure that showed higher photoactivity and greater current density for hydrogen intercalation compared to nonporous WO_3.[42] Feng et al. synthesized mesoporous WO_3 films based on a one-step electrodeposition approach.[44] They concluded that the presence of mesoporous WO_3 films greatly enhanced protein loadings,which illustrated that this type of film can provide high active surface area.

3. Effects of Synthesis Parameters on Nanostructures of WO_3

3.1. Metal oxide precursor

The metal oxide precursors used in the electrochemical synthesis route can significantly affect the morphology of nanostructures WO_3 films. Shen et al.,[31] found that WO_3 films electrodeposited from solutions containing an alcohol were more stable than the solutions without alcohols. Tsuchiya et al. synthesized WO_3 films by anodization in NaF-containing electrolytes.[28] They found that the morphology of WO_3 films was strongly affected by the NaF concentration in the precursor solution (Figure 3). Etching of the resulting metal oxide layers increased with increasing NaF concentration, causing the pores to coa-

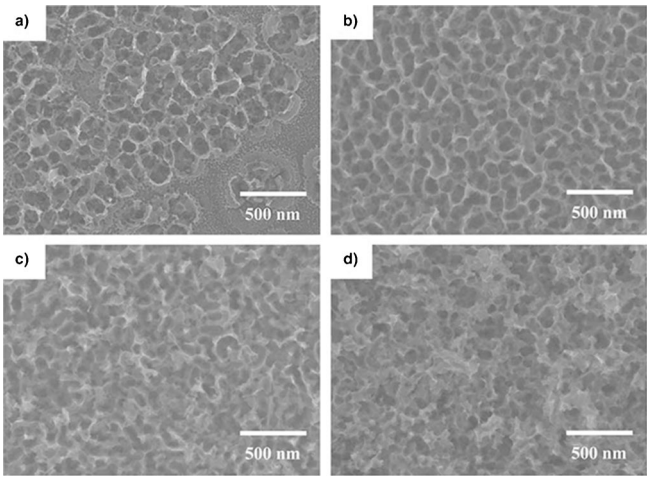

Figure 3. Plan-view SEM images of the porous layers formed at 60 V in various NaF electrolytes: a) 0.1, b) 0.2, c) 0.5, and d) 1.0 wt%. Reprinted from Ref. [28].

lesce as well as the oxide layers to exhibit a mesh-like structure.[28] Watcharenwong et al. prepared WO_3 films by anodization using different precursors and found that 0.15 M NaF will result in nanoporous WO_3 films; 0.3 M oxalic acid will cause WO_3 films to be partially or totally eroded; and PEG:H_2O (PEG = polyethylene glycol) will form aggregated WO_3 films.[13c] Zhang et al. found that the presence of NaF is beneficial for the formation of regular self-assembled nanoporous WO_3 structures, whereas planar films can be obtained without fluoride under the same anodization conditions.[8c]

The electrodeposition efficiency is also strongly influenced by the composition of precursors. Kondrachova et al. found that the efficiency of electrodeposition from a peroxo-polytungstate solution strongly depended on the composition of the precursors.[50] Apart from this, Yang et al., also found that the pH value of precursors played an important role in modifying the surface morphology of nanostructured thin films (Figure 4).[29] In their study, two different film types were obtained at three different pH values. A mesoporous WO_3 film formed when performing the electrodeposition under cyclic voltammetry (i.e., −0.8 to 0.2 V, 50 mV s^{-1}, three cycles) from a strongly acidic solution (pH 0.8; adjusted by using H_2SO_4). They found that the optimum pH range to prepare mesoporous WO_3 films was between pH 0.8–1.1, whereas transparent WO_3 films were electrodeposited from precursor solution (pH 1.92) but without the addition of H_2SO_4. Compared to the transparent WO_3 films, the nanoporous WO_3 films formed under the optimum pH conditions gave rise to photocurrent densities nearly three times that of transparent nanoporous films.[29]

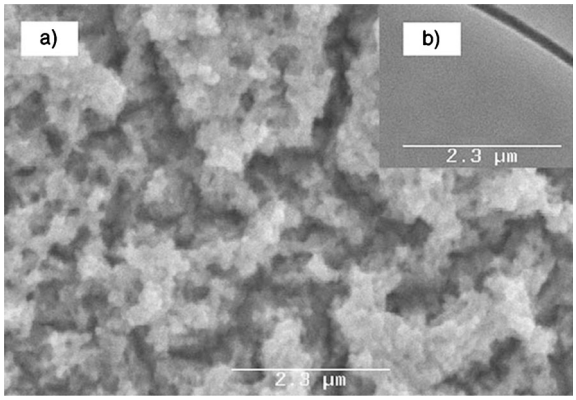

Figure 4. SEM images for the surfaces of a) mesoporous film prepared from electrolytes at pH 0.8 and b) transparent film deposited from electrolytes at pH 1.92. Reprinted from Ref. [29].

Thermodynamically, WO_3 (yellow) is reported to be stable in acidic environments. In strong acidic electrolytes, tungstate cations may be formed.[13a] Figure 5 shows that each applied potential represents a different region of the Pourbaix diagram in the investigation of pH influence on the behavior of W. The Pourbaix diagram shows the potential at which chemical and electrochemical reactions may occur on an electrode surface in a specific electrolyte as a function of the pH value.[51] The thermodynamic stability of chemical species at various potentials and pH ranges can also be determined from the Pourbaix diagram. W forms a wide range of oxides, and the most stable oxide is WO_3. Other oxides formed with W are mostly the results of thermal oxidation of W or reduction of WO_3. According to the Pourbaix diagram, the W surface at pH 2 should be passivated through the formation of WO_2, W_2O_5, or WO_3. Many researchers have studied the dissolution of tungsten oxides in acidic solution, but thus far no general agreement on the mechanism has been found. Di Paola et al. proposed a dissolution model for W in acidic solutions through the formation of intermediate species such as WO_2^{2+}.[52] For pH > 1, passive dissolution of W can occur owing to the conversion of species more stable than WO_2^{2+}, such as WO_4^{2-}. Anik et al. investigated the influence of the pH value on the anodic behavior of W.[53] They suggested that at pH 1 and pH 2.6, which corresponds to the point of zero charge of the WO_3 surface, both H^+ and H_2O would assist in WO_3 dissolution. When approaching pH 2.6, the contribution of H^+-assisted dissolution diminishes.[53]

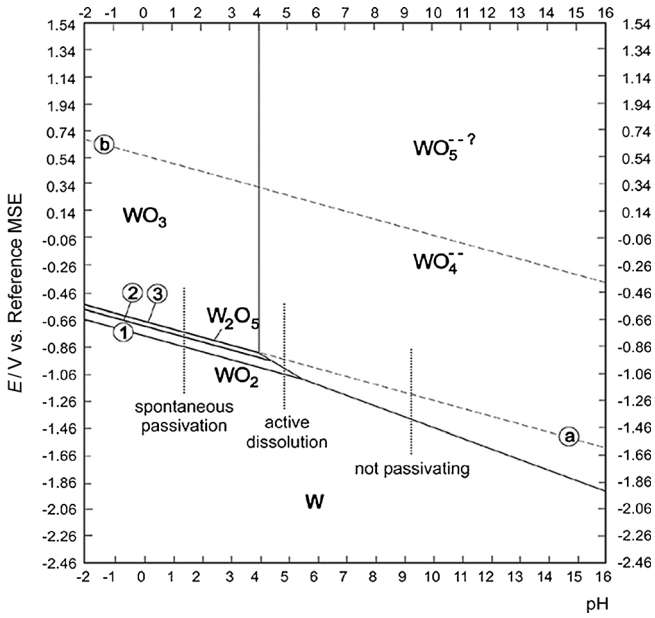

Figure 5. Pourbaix diagram for W (25 °C, [WO_4^{2-}] 10^{-6} mol L^{-1}). Line **a** shows the reduction equilibrium of water $E_{0,a} = -0.0591$ V × pH at a H_2 or O_2 pressure of 1 bar. Line **b** shows the oxidation equilibrium of water $E_{0,b} = 1.228$ V − 0.0591 V × pH. Reprinted from Ref. [54].

Leftheriotis and Yianoulis found an aging effect for the formation of WO_3 films after electrodeposition from the precursor solution.[33] The WO_3 films aged for 48 h after the electrodeposition had a considerably higher surface roughness. This was attributed to a conglomeration process, which is the dominant mechanism leading to the formation of grape-like structures that directly increase the surface roughness.[33]

Berger et al. prepared nanoporous WO_3 films by anodization in 1 M H_2SO_4 with 0.5 wt% NaF.[55] They found that the formation of the pore structure could be attributed to enhanced etching caused by F^- ions in the electrolyte, leading to a self-

ordering by competition of film formation and dissolution. Contrarily, Nah et al. synthesized compact WO_3 films by using the same method on W sheets in 1 M H_2SO_4 solution but without addition of NaF to the electrolyte solution.[56] Kwong et al. synthesized the WO_3 films from peroxotungstic acid solution containing different carboxylic acids (e.g., formic, oxalic, citric).[43] They found that the photocurrent densities of WO_3 films prepared with carboxylic acids dissolved in the electrolyte are greater than those of WO_3 films synthesized from pure peroxotungstic acid solution alone. The differences were attributed to improvements in (1) grain size, which controls the photogenerated electron–hole transport; and (2) effective grain boundary area, which controls the number of active reaction sites and electron–hole recombination sites.[43]

3.2. Electrode substrate

Various conductive electrode substrates have been used to provide an effective electrodeposition platform for the growth of nanostructured WO_3 thin films. In general, it can be summarized that the chosen electrode substrate can affect the final electrodeposition efficiency. In addition, the surface structure of the chosen electrode substrates has an impact on the eventual size, shape, and efficiency of WO_3 films formed. Thus, understanding the impact of the surface structure of chosen electrode substrates during the electrodeposition process are essential to achieve a more uniform particle size and better dispersion of photocatalyst particles.[57]

To date, the most common electrode substrates used in the electrochemical synthesis methods are ITO- and FTO-coated glass electrodes. Other electrode substrates have also been used in some studies.[57] Shen and Tseung synthesized WO_3 films by performing the electrodeposition method on various electrode substrates including ITO-coated glass, Au foil, and Pt foil.[31] They found that the highest surface coverage of WO_3 at the same current density and deposition charge was achieved on ITO-coated glass, followed by Au foil whereas the least coverage was on Pt foil. Wei and co-workers prepared WO_3/n-Cu_2O and WO_3/p-Cu_2O composite films on Ti electrode substrates using cathodic electrodeposition.[16] They first synthesized the WO_3 films on Ti electrodes followed by the n-Cu_2O or p-Cu_2O layer. Baeck et al. also synthesized WO_3 films by pulsed electrodeposition on Ti electrodes and ITO-coated glass electrodes.[49] When comparing the cathodic current deposition, the nanocrystalline WO_3 films on Ti electrodes showed significantly higher current densities.[49] Huang et al. fabricated WO_3-doped amorphous hydrogenated carbon films on Si as electrode substrates by using electrodeposition.[58] They found that the sizes of the nanocrystalline WO_3 particles were in the range of 8–12 nm and that the particles were homogeneously embedded in the amorphous carbon matrix. Watcharenwong et al. produced WO_3 films through cathodic electrodeposition on stainless-steel electrodes for PEC experiments.[13c] They found that the surface structure of stainless-steel electrodes significantly affected the size and morphology of WO_3 films formed. Lee et al. prepared WO_3 films on polished Ti sheets that showed a considerably enhanced photocurrent compared to WO_3 films on unpolished and preoxidized Ti sheets.[59] This finding suggested that the in situ formation of a thin WO_x–TiO_y interfacial composite layer and an improved adhesion of WO_3 to the polished Ti sheet played an important role in enhancing the photoresponse.[59] Pauporte developed a simplified approach for the electrodeposition of WO_3 films and found that the mass uptake on the Au electrode, as well as the nucleation process and adhesiveness of the films were poor.[40] However, he also reported that such problems were not encountered with FTO-coated glass electrodes.

3.3. Applied potential and current density

The morphology of nanostructured WO_3 films also strongly depends on the applied formation potential and current density. The applied potential during the anodization process is very important for the formation of regular nanoporous WO_3 thin films.[8c] Tsuchiya et al. reported the preparation of highly ordered porous WO_3 films by performing potentiostatic anodization on pure W in NaF electrolytes.[28] At higher applied potentials (i.e., 40–60 V), well-structured porous arrays were observed on almost all film surfaces. These arrays become larger with increasing applied potentials.[28] In addition, Watcharenwong et al. studied the synthesis of WO_3 films by anodization at different potentials in various electrolytes.[13c] In 0.15 M NaF electrolytes and an applied potential range of 20–60 V, the resulting morphologies of WO_3 films were nanohole like with structures resembling a highly porous honeycomb and large surface areas (Figure 6). In addition, the morphology of WO_3 films in oxalic acid as electrolyte changed from little etching features at 20 V to a partially carved oxide layer at 40 V, and finally to a completely etched-in oxide layer with a brain-like morphology at 60 V. However, the oxide films prepared at 80 V in 0.3 M oxalic acid electrolyte yielded the same nanoporous structure as those prepared from 60 V. In addition to the applied potentials and current densities, the anodization times also affected the morphology of the WO_3 films.[13c] Zhang et al. studied the anodization of W foil and found that the applied potentials either lower or higher than 40 V will produce nanoporous films instead of regular nonporous structures.[8c] Pauporte controlled the applied potentials in the range of $+0.06$ to -0.34 V (vs. NHE) in electrodeposition experiments using a precursor solution of 25 mM Na_2WO_4 and H_2O_2 acidified at pH 1.2 using $HClO_4$.[40] The highest deposition efficiency was found for a Na_2WO_4/H_2O_2 ratio of 0.8 and a deposition potential of -0.24 V (vs. NHE). De Tacconi et al. electrodeposited WO_3 and WO_3–TiO_2 composite films by pulsed electrical potentials at -0.45 and -0.95 V, respectively.[34] At -0.45 V, it was revealed that the pulsed potential promoted the incorporation of more TiO_2 into the composite films whereas the more negative pulsed potential resulted in only a negligible amount of TiO_2 in the composite film.[34]

It was also determined that different applied current densities could also affect the structure of WO_3 formed during the anodization. For instance, Mukherjee et al. prepared WO_3 films under galvanostatic anodization in a 0.25 M oxalic acid electrolyte and found that a nonporous film was formed at a current

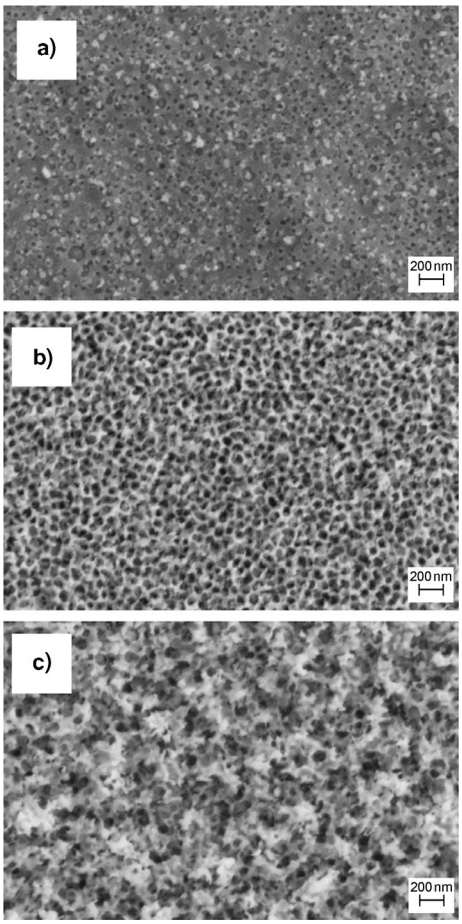

Figure 6. Effect of anodization voltage on the morphology of nanoporous WO_3 films as probed by SEM. The films were grown in 0.15 mol L^{-1} NaF for 3 h at a) 20, b) 40, and c) 60 V, respectively. Reprinted from Ref. [13c].

density of 2.75 mA cm^{-2}.[25] However, it was noted that the film behavior changed as the current density increased. At 5.86 mA cm^{-2}, a porous WO_3 film was observed and the porosity increased when the current was increased to 6.06 mA cm^{-2}. At the optimum current density of 6.94 mA cm^{-2}, the entire WO_3 film was transformed into a completely porous structure. A further increase in current density beyond 9.74 mA cm^{-2} resulted only in enlarged pores to (> 100 nm).[25]

It is also important to understand the implications of the different potential modes on the formation of nanostructured WO_3 films prepared by either sweeping or stepping potential modes. These potential modes will influence the physical properties of the metal oxide layers formed in terms of their density, porosity, and defects. When the sweeping potential mode (mild anodization) to relatively high formation potentials (up to 80 V) is applied, the formation of compact TiO_2 and WO_3 layers with thicknesses proportional to the applied potentials are observed. However, when the stepping mode is used, a completely different physiochemical process occurs. For instance, breakdown of WO_3 films takes place as a result of the high field strengths caused by the high applied potentials. As a direct effect, the formation of nanostructures was evident.[24] In an other study, Berger et al. obtained porous WO_3 layers through anodization at 40 V (measured against Ag/AgCl) for 1 h at a scan rate of 1000 mV s^{-1} in an electrolyte containing H_2SO_4 and NaF.[55] The synthesized WO_3 film showed a photocurrent efficiency significantly higher than a compact WO_3 layer with comparable light absorption length. In general, it was observed that WO_3 films of good adherence was obtained when electrodeposited at relatively low potentials. In addition, it was reported that the charge density is a function of the applied potential during the electrodeposition of $Mo_xW_{1-x}O_3$ films on ITO-coated glass electrodes. Kondrachova et al.,[50] observed that the electrodeposition rates of Mo from the precursor solution increased at more negative potentials.[50] Vijayalakshmi[17] prepared WO_3 films by galvanostatic deposition at constant current densities of 0.50, 0.65, and 0.75 mA cm^{-2}. Their results showed that the X-ray diffraction (XRD) peaks measured at $2\theta = 26.8^\circ$ and 45.30° attenuated with increasing current densities. In their study, they observed that the XRD peak measured at 0.50 mA cm^{-2} was reduced in intensity at 0.65 mA cm^{-2} whereas no prominent XRD peak was detected at 0.75 mA cm^{-2}.

Other effects of applied current density include the changes brought onto the weight ratio of W:O, as well as the band gap energy of nanostructured WO_3 films formed. It was found that the optical band gap energy for nanostructured WO_3 films decreased from 3.2 to 2.5 eV with current density increasing from 0.50 to 0.75 mA cm^{-2}.[17]

3.4. Annealing temperature

Annealing is required to transform the WO_3 film electrodeposited on the electrode substrate into a well-crystallized WO_3 film. Such a transformation process usually occurs at the expense of decreasing surface area and active sites for subsequent photocatalytic reactions.[60] When the electrodeposited WO_3 film is subjected to different annealing temperatures, the following phase transitions occur: triclinic (as-electrodeposited)→amorphous (100 °C)→triclinic (250 °C)→hexagonal (500 °C). After the electrodeposition process, the WO_3 film layers could be transformed into a monoclinic structure by thermal annealing.[56] Ng et al. determined the degree of crystallinity of the WO_3 electrodes annealed at different temperature and showed that the photocurrents and charge stored changed with the degree of crystallinity (Figures 7 and 8).[61] It was also observed that upon applying annealing temperatures at 250 and 500 °C, the morphology of WO_3 films will change to rod-, sheet-, and fibril-like structures.[55] Nah et al. assumed that both compact WO_3 (c-WO_3) and porous WO_3 (p-WO_3) have an amorphous structure and that they could be converted to the monoclinic WO_3 phase upon annealing.[56] While the annealing of c-WO_3 film layer caused a strong increase in the response time, the p-WO_3 film layer remained virtually unaffected by the crystallization process.[56] In addition, the change of the amorphous WO_3 layer to a monoclinic WO_3 layer on annealing at 500 °C was reported to significantly increase the photocurrent conversion efficiency as well as decrease the band gap energy.[55] In another study, it was reported that the shift in absorption edge of WO_3/TiO_2 nanoparticles depended not only

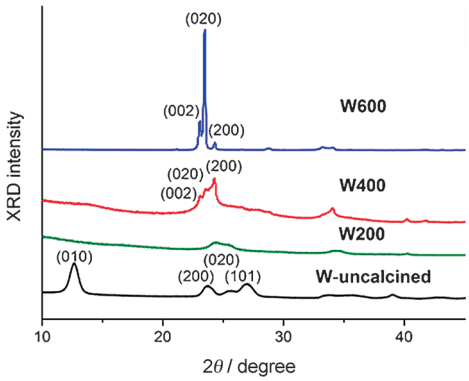

Figure 7. XRD patterns of WO_3 films at different calcination temperature of 200, 400, and 600 °C. Reprinted from Ref. [61].

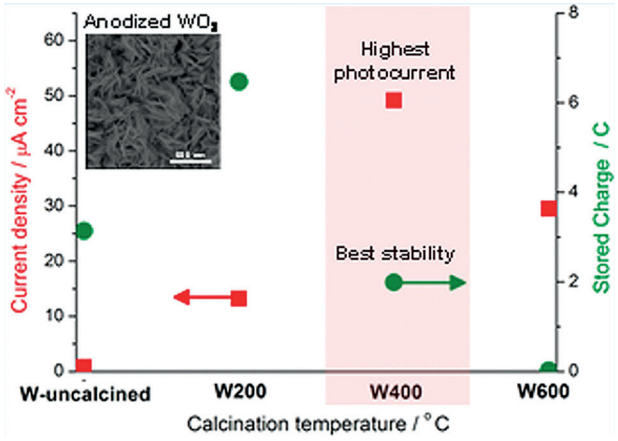

Figure 8. Photocurrent response for compact and porous WO_3 layers. The inset shows the SEM image for anodized WO_3 layer. Reprinted from Ref. [61].

on the synthesis method used and the nature of precursors but also more importantly on the type of thermal annealing treatment.[56]

When WO_3 and TiO_2 nanoparticles are coupled, the creation of defect energy levels within the forbidden band gap of WO_3 and TiO_2 reduces the total band gap energy by approximately 2% during thermal annealing.[56] Thus, annealing has indeed a profound effect on the morphology and physiochemical properties of the resulting WO_3 thin films. It was reported that the varying the annealing temperatures between 400–600 °C will gradually transform the morphologies of WO_3 films into different structures such as (1) a network of long needle-like particles of approximately 30 nm at 400 °C; (2) small plate-like particles of approximately 15 nm wide at 450 °C; and (3) larger nanoparticles with clearly observable pores in the range 500–550 °C.[13a]

Thermal annealing also has a significant influence on the particle size and photoactivity of annealed WO_3 thin films. Hong et al. found that the particle size increased with annealing temperature (Table 3).[63] Liu et al.[27] attributed the low photoactivity in annealed WO_3 thin films to the poor crystallization of the WO_3 samples. On increasing the annealing temperature to 450 °C, the photoactivity in WO_3 thin films was increased, which was linked to a higher degree of crystallization of WO_3 and a decrease in surface defects. They also reported that 450 °C was the optimum annealing temperature with the highest photoactivity and a reaction rate constant k of 0.0459 min^{-1} for PEC water splitting. Any further increase in annealing temperature beyond 450 °C caused a deterioration in the photoactivity of the WO_3 films.[27] Liu et al. ascribed the deterioration in photoactivity of WO_3 films to two main underlying causes:[27] (1) W_2N formed in the WO_3 films, which has a lower photoactivity; and (2) destruction of the nanoporous WO_3 films, which results in a decrease in photoactivity. Overall, it could be generalized that the crystallite sizes of WO_3 increased with annealing temperature.[63] In another study, when the annealing temperatures were varied between 500 and 800 °C, the WO_3 crystallite sizes increased from 30 to 500 nm.[62]

Table 3. The surface area and particle size of four different samples.[62]

Sample	BET area[a] [m^2g^{-1}]	Particle size [nm] BET	SEM	XRD
500 °C	21.3	39	30	37
600 °C	12.5	67	60	60
700 °C	2.2	380	200	76
800 °C	2.0	418	500	129

[a] Determined using the Brunauer–Emmett–Teller method.

Finally, annealing times also affect the properties of WO_3 films. Regragui et al. stated that the effects of annealing time on the structure and optical properties are significant.[64] The water content decreased significantly during annealing. FTIR spectroscopy and compositional measurements show that the un-annealed films have hydroxyl groups on the surface whereas water molecules are present in the bulk of the sample. During annealing, the hydroxyl groups are first destroyed and the water molecules leave the film as the annealing time is increased. The water evaporation during annealing results in a rough surface and causes the formation of defects; this results in an increase of light scattering as demonstrated by optical measurements. Thus, a significant decrease in light scattering was observed when the annealing time decreased.[64]

3.5. Film composition

To date, the photocatalytic characteristics of nanostructures WO_3 have not been studied as extensively as that of TiO_2. A previous study revealed that WO_3 is not an effective photocatalyst.[63] One of the possible reasons may be owed to the fast recombination rate of electron–hole pairs photogenerated in WO_3, which lowers the photocatalytic efficiency.[65] An effective approach to increase the efficiency of charge separation usually involved the coupling of two or more semiconducting metal oxides with different band gap energy levels. Many studies have indicated that coupling WO_3 with other semiconductors with a broader band gap energy, such as TiO_2 and ZnO, will result in a better separation of charge carriers. Recently,

the coupling of WO_3 with semiconductors having lower band gap energies has attracted considerable attention; these include $CaFe_2O_4$ (1.85 eV), Fe_2O_3 (1.97 eV), $BiVO_4$ (2.4 eV), $CuBi_2O_4$ (1.5 eV), and CdS (2.25 eV).[16] In a composite semiconductor with a bilayer structure, the amount (or thickness) of coating, usually the upper layer of the composite film, plays an important role in enhancing the photoactivity. Saito et al. synthesized a very thin SnO_2 layer sandwiched between $BiVO_4$ and WO_3 layers in a carbonate electrolyte and found that the solar energy conversion efficiency reached approximately 0.9–1.35% using single- or double-stacked photoanodes, respectively.[66] They also found that the photocurrent was further enhanced by the insertion of SnO_2 sandwich layer (Figure 9). Mi et al. reported stable intercalation compounds with the composition $xN_2{\cdot}WO_3$ ($x = 0.034$–0.039).[10a] The compound was formed by trapping N_2 in WO_3; they also established that WO_3 intercalated with N_2 gas exhibited a narrower band gap than pure WO_3.[10a]

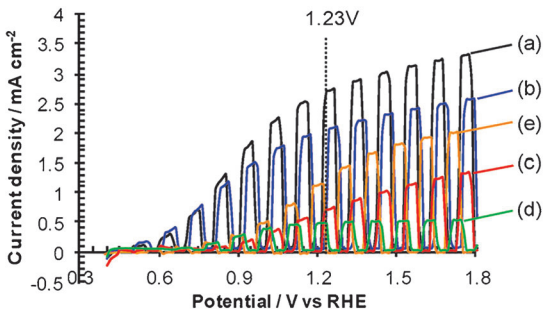

Figure 9. *I–V* curves of multicomposite film, bare $BiVO_4$, and bare WO_3 photoelectrodes: a) $BiVO_4/SnO_2/WO_3$, b) $BiVO_4/WO_3$, c) bare $BiVO_4$, d) bare WO_3 in 0.1 M $KHCO_3$ aqueous solution, and e) $BiVO_4/SnO_2/WO_3$ in 0.1 mol L^{-1} Na_2SO_4 aqueous solution. Reprinted from Ref. [66].

De Tacconi et al. prepared WO_3/TiO_2 thin films using a pulsed deposition technique and found that the resulting composite films had a superior PEC performance in 0.1 M Na_2SO_4 relative to the individual component oxides of WO_3 and TiO_2.[34] The incident photon-to-electron conversion efficiency (IPCE)[21c,67] was determined by the mathematical expression given by Equation (8):

$$\mathrm{IPCE} = \left[\frac{1240 \times I}{\lambda \times P}\right] \times 100\,\% \qquad (8)$$

where λ (nm) is the wavelength of incident light, P (mW cm^{-1}) is the illumination power density at the specific wavelength and I (mA cm^{-1}) is the measured short circuit photocurrent density at the same wavelength. In this study, the IPCE for the WO_3/TiO_2 composite films was double that of its parent individual component oxides in the range 250–320 nm. The increase in IPCE was mainly attributed to the spatial separation of photogenerated electron–hole pairs, which resulted in minimal recombination of electron–hole pairs. Other contributions such as interparticle connection and electron percolation pathways in the WO_3/TiO_2 composite films were also considered as reasons for the enhanced IPCE. Moreover, the element ratio of the composite also has a strong effect on the photocatalytic activity. Leonard et al. found that adding 9% Zn to W resulted in a over 2.5-fold increase in photocurrent for both sulfite and water oxidation (Figure 10).[68] Yagi et al. reported a unique approach for the synthesis of $WO_3/[Ru(bpy)_3]^{2+}$/PSS composite films, that is, simple electrodeposition from a colloidal solution containing peroxotungstic acid and $[Ru(bpy)_3]^{2+}$ stabilized by PSS.[69] Kondrachova et al. prepared mixed Mo–WO_3 films of varying stoichiometric ratios through cathodic electrodeposition on ITO-coated glass electrodes from aqueous peroxo-polymolybdotungstate solutions.[50] Liu et al. prepared WO_3 by anodization prior to doping with N by annealing the WO_3 films in NH_3/N_2.[27] They found that the IPCE of N-doped nanoporous WO_3 films showed a significant enhancement in the energy conversion efficiency under visible light. This showed that the modification of WO_3 films with N could improve the water electrolysis process. In another study, it was found that the modification of WO_3 films with Ag–Bi resulted in a reduction of the band gap energy. They observed that the O_2-evolving overpotential decreased from 318 to 290 mV at a current density of 1 mA cm^{-2}. In this instance, WO_3 played an important role in improving the performance of the Ag–Bi catalyst for oxygen evolution and, thus, resulted in an improved photoactivity in the composite WO_3/Ag–Bi films.[36] Wei et al. synthesized WO_3/n-Cu_2O and WO_3/p-Cu_2O composite films by consecutive cathodic electrodeposition and found that the photoactivity of WO_3/p-Cu_2O was higher than that of pure WO_3 and p-Cu_2O alone.[16] On the other hand, the photoactivity of WO_3/n-

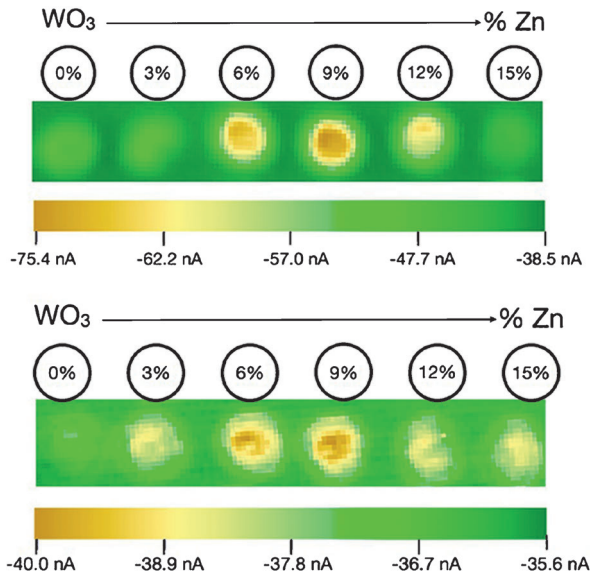

Figure 10. SECM images for the typical photocurrent response of Zn/WO_3 composites a) under full UV irradiation and b) with a 420 nm long-pass filter. The color represents the measured photocurrent shown in the scale bar below each SECM image. Also shown is a schematic depicting the amount of Zn (in percent) in each spot in the array electrode. The photocurrent shown is for sulfite oxidation (0.1 mol L^{-1} Na_2SO_4 + 0.1 mol L^{-1} Na_2SO_3 at pH 7) measured at an applied potential of +0.2 V vs Ag/AgCl. Reprinted from Ref. [68].

Cu_2O was higher than that of pure WO_3 but lower than n-Cu_2O.

Figure 11 shows a diagram of the charge-transfer process in WO_3/n-Cu_2O composite films. Thermodynamically, the photogenerated electrons are transferred from the conduction band of n-Cu_2O to that of WO_3 in the WO_3/n-Cu_2O composite films;

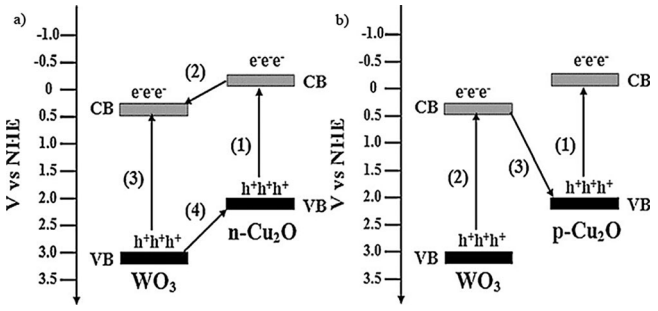

Figure 11. Schematic diagrams for charge-transfer process in a) WO_3/n-Cu_2O composite film and b) WO_3/p-Cu_2O composite film. Reprinted from Ref. [16].

this made it impossible for the adsorbed O_2 to consume the transferred electrons. Therefore, the WO_3/n-Cu_2O composite films exhibited a lower photoactivity than n-Cu_2O alone. As for the WO_3/p-Cu_2O composite films, the charge-transfer process could be explained by the p–n photochemical diode in Figure 11 B. The majority of electrons in WO_3 and holes in p-Cu_2O recombine by charge transfer through the interfaces between the two semiconductors, but the recombination of the photogenerated charges in the respective semiconductors is suppressed. Thus, the photogenerated electrons with strong reduction power will accumulate in the conduction band (Cu_2O) as well as leave the relative photogenerated holes with strong oxidation power in the valence band (WO_3).

Leonard et al. studied the space-charge capacitance by electrochemical impedance spectroscopy to obtain Mott–Schottky plots based on WO_3 films (Figure 12).[68] They obtained flat band potentials of each semiconductor material using the Mott–Schottky equation at 298 K. The flat band potential could be estimated from the *x*-axis intercept of the linear portion of the Mott–Schottky plots. An average of the *x*-axis intercepts, at three different frequencies, produced flat band potentials for WO_3 that were determined to be 0.64 V (vs. NHE, with an estimated precision of ± 0.1 V). As is frequently the case, flat band potentials obtained from Mott–Schottky plots show a frequency dependency that may originate from surface roughness or from the many grain boundaries in the drop-cast semiconductor films.

Wang et al. reported that the photostability and photoactivity of WO_3 for water oxidation can be simultaneously enhanced by controlled introduction of oxygen vacancies into WO_3 in a H_2 atmosphere at elevated temperatures.[70] To investigate the effect of hydrogen treatment on the electronic properties of WO_3, they measured the electrochemical impedance and derived the capacitances for the Mott–Schottky plot shown in Figure 13. In general, samples show positive slopes in the Mott–Schottky plots for n-type semiconductors. The hydrogen-treated WO_3 samples show substantially smaller slopes compared to the untreated WO_3 sample, suggesting significantly increased donor vacancies densities based on the Mott–Schottky equation. The enhanced donor density is attributed to the introduction of oxygen vacancies, which serve as shallow electron donors, which improves the charge transport in WO_{3-x} and at the interface between substrate and WO_{3-x}. Furthermore, the capacitance of pristine WO_3 reaches a plateau at around 0.2 V (vs. Ag/AgCl), which suggests that the depletion layer does not increase with further increase of applied potential. This explains the saturation of the photocurrent density at around 0.2 V (vs. Ag/AgCl). There is a also negative shift of the flat band potential in the H_2-treated samples, possible caused by the substantially increased donor density that shifts the Fermi level of WO_3 upward. Additionally, the contribution of the Helmholtz layer capacitance becomes significant when the donor density of WO_3 increases by three orders of magnitude increase, which will cause a negative shift of the flat band potential in the Mott–Schottky plot as well.

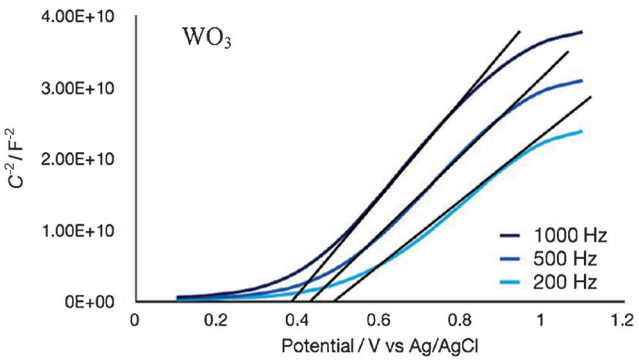

Figure 12. Mott–Schottky plot at frequencies of 200, 500, and 1000 Hz for WO_3 in 0.1 mol L^{-1} Na_2SO_4 at pH 7 obtained from electrochemical impedance spectroscopy. The *x*-intercept of the linear region (black lines) shows the measured flat-band potential. Reprinted from Ref. [68].

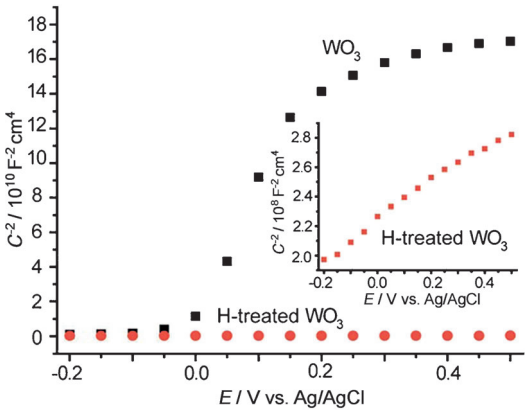

Figure 13. Mott–Schottky plot for WO_3 and hydrogen-treated WO_3 sample prepared at 350 °C and a frequency of 10 kHz in the dark. Inset: magnified Mott–Schottky plot of the hydrogen-treated WO_3. Reprinted from Ref. [70].

3.6. Size and thickness

It was known from previous studies that the catalytic activity of nanostructured WO_3 is also affected by the size, shape, and thickness of the photocatalyst particles.[71] Nanoscaling is an effective method for increasing the energy difference between the band edges and redox levels as a result of quantum size effects.[72] A small WO_3 crystal size enhances the photoactivity by increasing the catalytic surface area. However, a small particle size also increases the rate of charge recombination due to copious amounts of surface defects. Therefore, the optimum WO_3 crystal sizes have to be a compromise between optimum catalytic surface area and the rate of surface charge recombination. Studies by Kwong et al. also supported the assumption that optimizing the WO_3 crystal size is important for PEC water splitting applications.[43]

In general, semiconductor nanoparticles with high photoactivity and strong quantum-size effect are considered to be superior photocatalysts.[60] It is well-established that the PEC water splitting efficiency of nanostructured WO_3 can be enhanced by improving crystallinity, grain size, film thickness, surface morphology, and catalytic surface area.[59] As discussed in previous sections, different synthesis approaches will yield nanostructured WO_3 with different morphologies and structures. A variety of morphologies and nanostructures can be obtained by varying the starting materials and solution chemistry, applied potential and current density, thermal annealing treatment and other synthesis factors.[33]

Xu et al. determined that nanoporous WO_3 films have a better PEC and photocatalytic performance than planar WO_3 films.[8c] Hong et al., synthesized monoclinic WO_3 nanocrystals via the hydrothermal reaction followed by post-calcination treatment.[62] They found that the WO_3 particle sizes varied from 30 to 500 nm as the calcination temperatures was changed from 500 to 800 °C. In another study, the average grain sizes were related to the amount of hydronium ions and molecular weight of additive.[13a] Gao et al. observed improved physical and chemical properties in nanostructured metal chalcogenides owing to quantum size effects when the particle size was reduced on the nanometer scale.[74] Previously, a number of excellent review articles on the synthesis of nanostructured metal chalcogenides with controlled particle size and shape have been published.[75] Generally, the size and morphology of a specific metal chalcogenide could be effectively controlled by judicious adjustment of a number of synthesis factors such as the type and ratio of starting reagents, reaction temperature, reaction time, and aging period. For the hydrothermal method, the presence of a small quantity of organic ligands often plays a key role in determining the size, shape, and structure of the metal chalcogenides formed.[74] After the hydrothermal reaction, a high-temperature calcination treatment is usually used to remove the residual organic ligands, which could extensively alter the size and morphology of nanoparticles and in turn lower their photoactivity.[76] Although the reduction in particle size is beneficial for surface-dependent photocatalysis reactions (it leads to quadratic growth of specific surface area and catalytic reactive sites), it is not always true that a smaller particle size will result in a higher PEC water splitting efficiency (Figure 14). If the featured size, particularly of a spherical particle, is comparable with the electron mean free path, a strong quantum confinement effect appears to increase the probability of the recombination of photogenerated electron–hole pairs.[65] Normally, a thin film can

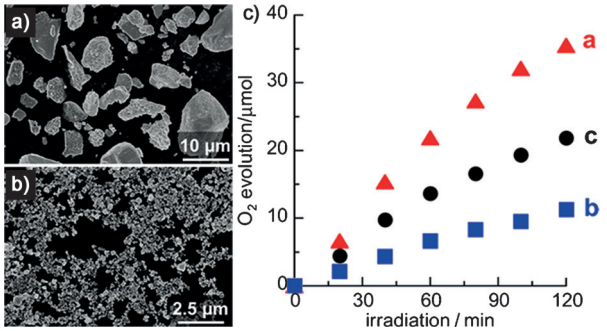

Figure 14. SEM images of a) large and b) fine WO_3 particles classified from WO_3 (K). Time courses for the photocatalytic evolution of oxygen over A) WO_3 (KL), B) WO_3 (KF), and C) commercial WO_3 (K) under irradiation (405 nm). Reprinted from Ref. [73].

prevent the scattering of light and enhance the transmittance of light, but immobilization of the thin film form would lead to surface area constraints. Thus, suspended catalysts usually have higher surface areas than films/supported ones and the intrinsic photocatalytic activity of powders is usually higher than that of films. Kwong et al.[12a] determined that the size of WO_3 grains is dominated by the precursor W concentration and not by the deposition time. On the contrary, the film thickness depends on both precursor W concentration and deposition time, and the PEC water splitting efficiency is known to increase with increasing film thickness. Such a positive trend in PEC water efficiency was attributed to the fact that thicker WO_3 films will cause a reduction in the band gap energy while increasing the light absorption (Figure 15).[12a]

It was also found that the nanostructured WO_3 film thickness could be increased with the aid of illumination. Kim et al. found that the thickness of nanostructured WO_3 could be extended to more than 2.6 µm by using the photochemical anodization method, which is double the typical film thickness obtainable by conventional anodization methods without illumination.[22b] Baeck et al. applied pulsed electrodeposition to synthesize WO_3 films with particle sizes between 45 and 330 nm and found that the cathodic deposition voltage (−1 to −3 V) had little effect on the particle size.[49] Generally, shorter electrodeposition pulses increased the nucleation rate for new particles above the growth rate of existing particles, which would explain the observed variation in particle size (Figure 16). It was found that the particle sizes were independent of the total number of electrodeposition pulses applied; it seemed to affect the WO_3 film thickness but not the final particle size.[49] Riboni et al. found that the size of nanoparticles formed was a function of the W/Ti ratio and the particle that the size decreased with an increase in the amount of W used.[77]

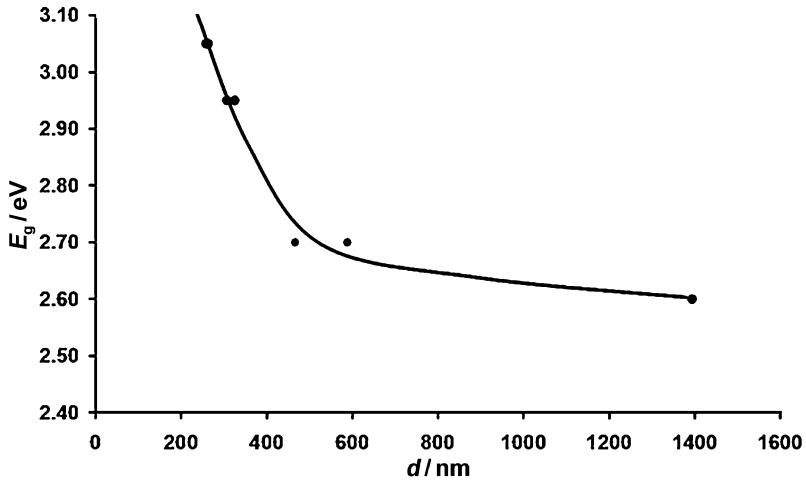

Figure 15. Optical indirect band gap (E_g) of WO_3 thin films as a function of thickness (*d*). Reprinted from Ref. [12a].

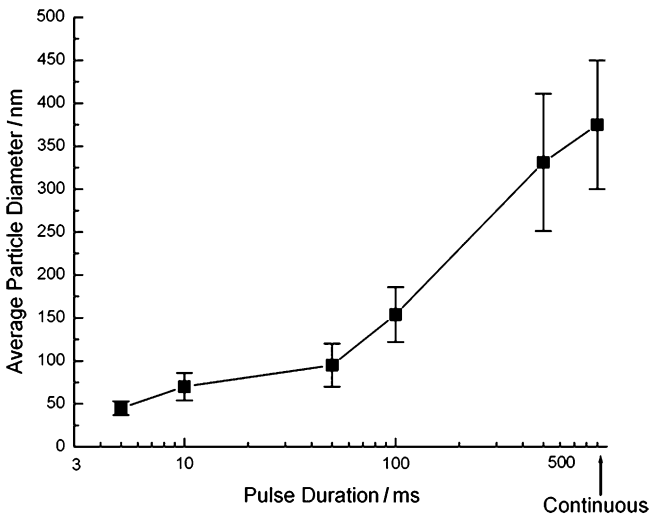

Figure 16. Dependence of particle size of tungsten oxide films on pulse duration. Error bars indicate one standard deviation above and below the mean. Reprinted from Ref. [49].

4. Fundamental Principle of WO_3-based PEC Water Splitting

In general, a photocatalysis cycle is comprised of three key steps:[78] (1) light illumination-induced transition of electrons from the valence band to the conduction, leaving an equal number of vacant holes; (2) migration of excited electrons and holes to the photocatalyst surface; and (3) reaction with adsorbed electron donors (D) and electron acceptors (A). Light absorption and the resulting photo-excitation of electron–hole pairs take place when the energy of incident photons matches or exceeds the band gap energy of semiconductor photocatalysts. In semiconducting photocatalysts, the conduction-band electrons (e_{CB}^-) possess an electrochemical chemical potential between +0.5 and −1.5 V (vs. NHE); therefore, they can act as reductants. The valence-band holes (h_{VB}^+) usually exhibit a strong oxidative potential between +1.0 and +3.5 V (vs. NHE).

Initially, the energy of incident photons is stored in semiconducting photocatalysts through photo-excitation and is later converted into chemical energy through a series of electronic processes and surface/interface reactions. Theoretically, a Gibbs free energy change ΔG° of 237 kJ mol^{-1} or 1.23 eV is needed to drive the overall reaction and to account for the overpotential losses occurring at both the anode and cathode caused by the water splitting reaction.[80] In contrast to the thermodynamics of conventional catalysis, photocatalysis can promote not only spontaneous reactions ($\Delta G<0$) but also nonspontaneous reactions ($\Delta G>0$). In the former case ($\Delta G<0$), the input energy is used to overcome the activation energy barrier (E_b). In the latter case ($\Delta G>0$), a part of the input energy is converted into chemical energy that is accumulated in the form of reaction products or by-products. However, WO_3 has strong oxidizing ability, which can be largely explained by its poor band alignment with respect to the reversible hydrogen electrode (RHE). For this reason, a bias voltage must be applied to the WO_3 photoanode to achieve H_2 evolution at the PEC cathode.[81]

In a second step, a large proportion of electron–hole pairs usually recombine, dissipating input energy in the form of heat or light emission. To prevent the recombination of electron–hole pairs, the co-catalyst strategy has generally been applied, that is, loading metal co-catalysts such as Pt,[83] Pd,[84] NiO,[85] and RuO_2[86] onto the semiconductor surface or within the lattice network. The heterojunctions formed between the host semiconducting photocatalysts and co-catalysts provide an internal electric field and/or circuit that facilitates separation of the electron–hole pairs and induces faster migration of charged carriers.[87] Furthermore, the presence of co-catalysts usually enables a higher conductivity and photoactivity while lowering the overpotential of the host semiconducting photocatalysts themselves. Thus, the co-catalysts often provide ideal active sites for photocatalytic reactions to proceed.[65]

Figure 17 shows the principle operation of WO_3 as a photocatalyst for water splitting in a PEC device setup. If WO_3 is used as the photoanode in the PEC device setup, Pt is often used as the cathode. Upon light illumination, the electrons in the valence band of WO_3 are promoted to the conduction band and transferred to the cathode (Pt) with the aid of an external bias. The transferred electrons will be used at cathode to reduce water molecules into H_2 and O_2. Simultaneously, the oxidation of water molecules is taking place at the WO_3 photoanode as the valence band holes are transferred to the electrolyte. To complete a PEC cell, three different configurations are possible

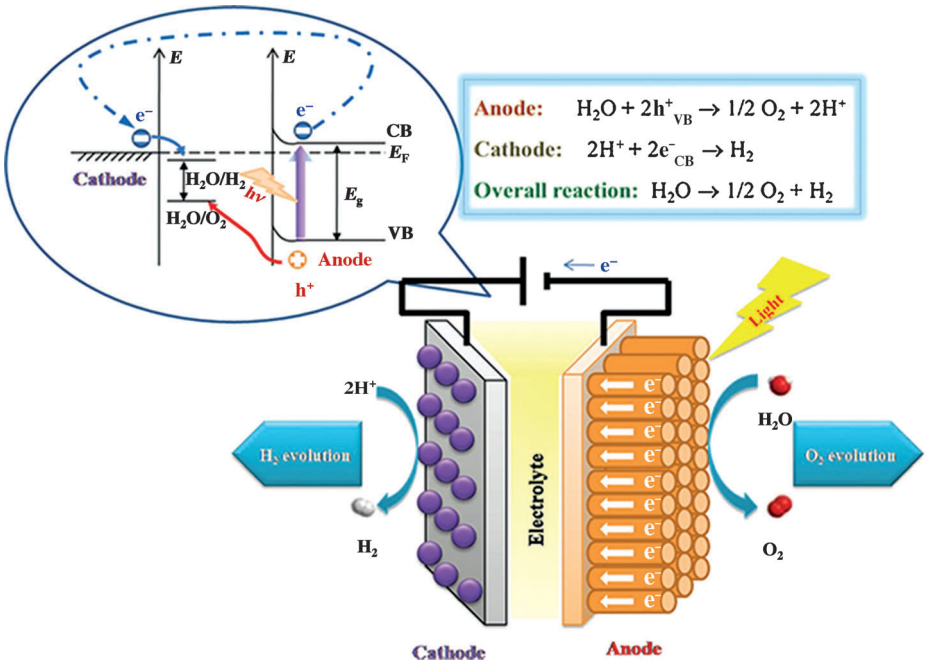

Figure 17. Schematic representation of a PEC device for H_2 and O_2 evolution. The inset represents the corresponding energy diagram for an n-type semiconductor and a metal as photoanode and photocathode, respectively. E_F indicates the Fermi energy level. Reprinted from Ref. [79].

and are shown in Figure 18. The fabrication, morphology, and photocatalytic performance of WO_3 has been generalized.[63] Its valence band edge can provide enough potential for O_2 production because it is located at approximately 3.0 eV versus NHE. However, WO_3 does not possess a high enough minimum conduction band for spontaneous H^+ reduction. Thus, it can be coupled with a photocathode (i.e., p-type semiconductor) suited for solar H_2 production in the form of a photoelectrochemical diode or a tandem device to achieve overall water splitting.[8a]

5. Evaluation Methods for Energy Conversion Efficiency of WO_3 Films

Chen et al. reported that the solar-to-hydrogen (STH) efficiency is the most important among the various efficiency measurements.[47] It is the only efficiency measurement method that can be used to determine the H_2 conversion efficiency from water splitting and, thus, should be used as the benchmark for comparison of different semiconductor PEC materials. The STH efficiency is given by Equation (9):[47]

$$\eta = \frac{\Delta G R_{H_2} - I V}{P_r A} \tag{9}$$

where η is the STH conversion efficiency after deducting the contribution from electricity. ΔG is the Gibbs free energy of the water splitting reaction. $R_{H_2}$is the rate of H_2 evolution estimated from the plot of accumulated H_2 yield versus reaction time. I is the measured electrical current during the reaction monitored by using an electrochemical workstation. V is the bias applied across the photocathode and photoanode in a two-electrode electrochemical cell. P_r is the intensity of light irradiation per unit area, either from a Xenon lamp or solar irradiation. A is the geometrical area of photoelectrode exposed to light irradiation. Equation (9) describes the overall efficiency of a PEC water-splitting device exposed to broadband solar Air Mass 1.5 Global (AM 1.5G) illumination under zero bias conditions. Zero bias implies that there is no applied voltage between the working electrode and counter electrode. However, WO_3 has exhibited poor PEC performance as a stand-alone photocatalyst largely due to the low band alignment when compared to the RHE. For this reason, a bias voltage must be applied to the WO_3 photoanode to achieve H_2 evolution at the photocathode. Thus, the STH efficiency measurement has been rarely used in previous studies when dealing with WO_3 photocatalyst.

In comparison, the incident photons-to-current (IPCE) efficiency [Eq. (8)] measurement has been widely used in previous studies.[21c,67] By definition, IPCE refers to the number of collected electrons per number of incident photons at a given irradiation wavelength. The photocurrent is one of the important parameters used in the IPCE equation. Ahmed et al. explained the photocurrent process in detail using as-deposited and annealed commercial nano-WO_3 on ITO-coated glass as electrode substrate immersed in 3 M NaCl.[88] Once a photostationary state is reached, the photogenerated holes will react with chloride leading to a net anodic photocurrent with electrons reaching the underlying ITO electrode surface. Thus, the photocurrent is affected by the presence of ions in the solution. Solarska et al. observed and also discussed the behavior of nanostructured WO_3 thin films deposited on photoanodes in methane sulfonic acid solution, which allows the generation of large and perfectly stable visible light-driven water splitting photocurrents.[89] In addition, they also studied the effect of electrolyte concentration upon current distribution and related photocurrent losses within the nanoporous WO_3 thin films on photoelectrodes. The electrolyte concentration for the photoanode in PEC cells will affect the photocurrent (Figure 19).

Saito et al. investigated the solar energy conversion efficiency of $BiVO_4/SnO_2/WO_3$ multilayers in highly concentrated carbonate electrolyte aqueous solutions.[66] They found that in the multi-composite $BiVO_4/SnO_2/WO_3$ layers on the photoanode, the photocurrent at 1.23 V (vs. RHE) in 0.1 M carbonate electrolyte solution was more than 2.4 times higher than that in sul-

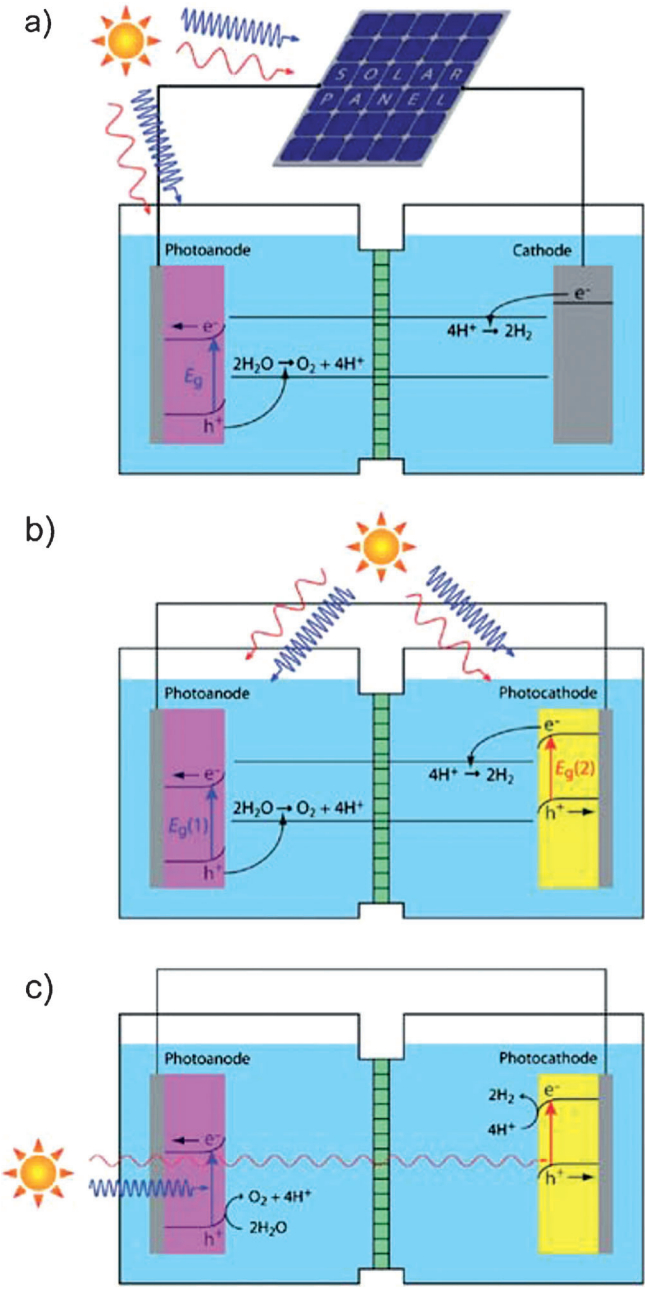

Figure 18. Three approaches to PEC solar water splitting: a) single-photoelectrode PEC cell assisted by a photovoltaic (PV) cell. Here, the photoanode is an n-type semiconductor with a positive valence band edge relative to the water oxidation potential. The PV cell boosts the potential of photogenerated electrons to allow water reduction at the cathode surface. b) Two-photoelectrode PEC cell in which the photoanode and photocathode are suitably matched n-type and p-type semiconductors assembled in parallel. c) A tandem two-photoelectrode PEC cell assembled in series, such that low-energy photons that are not absorbed by the photoanode are absorbed by the photocathode. Reprinted from Ref. [82].

fate electrolyte solutions. They concluded that the carbonate electrolyte solution is very effective in the case of multi-composite layers on photoelectrodes as well as in the case of a pure $BiVO_4$ layer.[66] Ishihara et al.,[6] found that the chemical nature of electrolytes played a crucial role in the efficient operation and energy conversion of a solar PEC cell. The interaction

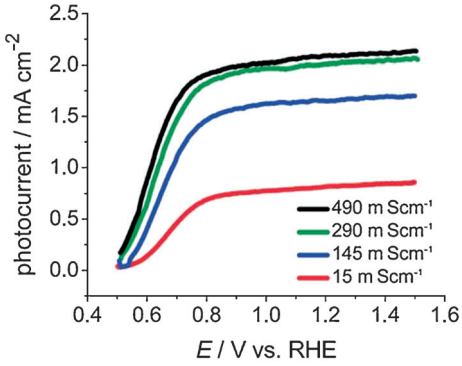

Figure 19. A series of photocurrent–voltage plots for the same electrode illuminated with AM 1.5 light in CH_3HSO_3 solutions of various concentrations: 2, 1, 0.5, and 0.04 mol L^{-1}. Reprinted from Ref. [89].

between the photoelectrode and electrolyte at the interface depended on the electrode types. They characterized nanoporous WO_3 structures based on their PEC properties in three different alkaline electrolytes (NaOH-based, KOH-based, and a mixture of NaOH and KOH-based electrolytes) and observed different photocurrent responses.[6]

Hill and Choi[46] studied the various effects of different anions and cations contained in an electrolyte solution on the photocurrent conversion efficiency (Table 4). They found that when $CH_3CO_2^-$ and Cl^- ions are present, the oxidation of $CH_3CO_2^-$ and Cl^- will become the dominant photooxidation reactions and completely suppress the O_2 evolution. When a PO_4^{3-} solution was used, the O_2 evolution and formation of

Table 4. Summary of the photocurrent to oxygen conversion efficiencies obtained in electrolytes with very pH conditions and anions (or cations).[46]

Electrolyte	pH value	Photocurrent-to-oxygen conversion efficiency [%]
CH_3COOH	3	0
CH_3COONa	5	0
NaCl	1	0
NaCl	3	0
NaCl	5	0
NaH_2PO_4	1	33
NaH_2PO_4	3	58
NaH_2PO_4	5	79
$NaClO_4$	1	32
$NaClO_4$	3	29
$NaClO_4$	5	9
Na_2SO_4	1	35
Na_2SO_4	3	63
Na_2SO_4	5	88
Li2SO4	3	35
Na_2SO_4	3	63
K_2SO_4	3	79
$LiClO_4$	3	10
$NaClO_4$	3	29
$KClO_4$	3	49
LiH_2PO_4	3	63
NaH_2PO_4	3	67
KH_2PO_4	3	87

peroxo species from water oxidation are the two major photooxidation reactions. The photocurrent-to-O_2 conversion efficiency in a PO_4^{3-} solution depends on the pH value; the efficiency was found to increase gradually as the pH value increases. When a SO_4^{2-} solution was used, the photooxidation of SO_4^{2-} to persulfate could also compete with the oxidation of water to O_2 and peroxo species. When the pH value of SO_4^{2-} solution is increased, the photocurrent-to-O_2 conversion efficiency will also increase, indicating that an increase in the pH value will improve the kinetics of O_2 evolution more than the kinetics of peroxo formation or sulfate oxidation. In PO_4^{3-}, SO_4^{2-}, and ClO_4^- solutions at pH 3, the highest photocurrent-to-O_2 conversion efficiency was obtained with K^+ ions whereas the lowest conversion efficiency was obtained with Li^+ ions.[46] Somasundaram et al. found that formate (HCO_2^-) is a more potent scavenger of photogenerated holes in semiconducting metal oxide films than either the adsorbed hydroxyl groups or water molecules.[48] The photocurrent enhancement on formate addition occurs partly because of the doubling in photocurrent responses as elaborated elsewhere.[48] Another key reason that makes it rather difficult to assess and compare the adopted synthesis methods is attributable to the utilization of various light sources for the PEC water splitting reaction in different studies.[12a]

Several reviews have been published on the numerous evaluation methods used to estimate the energy conversion efficiency of nanostructured WO_3 films formed from different synthesis methods.[13] Generally, it was found that the estimation of energy conversion efficiency in most of the studies involving nanostructured WO_3 was not a simple and straightforward task, which makes it rather difficult to assess and compare the adopted synthesis methods. However, it was reported that IPCE is valuable for understanding and improving material performance although the real energy conversion efficiency of the materials is not entirely reflected. To allow for an easy direct comparison between studies, we provide some suggestions: (1) it is encouraged to obtain materials in solutions using the same pH values; (2) the electrolyte solution should not contain any sacrificial donors or acceptors as the presence of any redox reactions will not reflect the true water splitting activity; and (3) the illumination source should closely match the shape and intensity of the AM 1.5G G173 standard set forth by the American Society of Testing and Materials. With these, it is anticipated that a standardized reporting method could be adopted by scientists and researchers in their future studies for correlating the synthesis method to the resulting energy conversion efficiency in PEC water splitting.

6. Recent Developments and Future Challenges

According to the discussion above, the size, thickness, composition, and physicochemical properties of nanostructured WO_3 can be easily tuned by adjusting the electrochemical synthesis conditions such as metal oxide precursor, electrode substrate, applied potential and current density, and annealing temperature. However, a successful breakthrough with regard to highly improved photoactivity of nanostructured WO_3 has not been achieved. In recent years, many efforts have been devoted to enhance the photoactivity of nanostructured WO_3, including the development of new light-harvesting assemblies, elucidation of charge-transfer processes, co-catalysts, and Z-scheme (i.e., splitting water into H_2 and O_2 using two different semiconductor photocatalysts) for improved H_2 production. In addition, the introduction of dopants into semiconductors can extend the photoresponse under visible light and has also been investigated, but this approach has produced limited success. Another effort is the coupling of semiconductors with sensitizing dyes that extends the concept of dye-sensitized solar cells into the photoelectrolysis systems. For instance, Brillet et al. presented a device based on an oxide photoanode and a dye-sensitized solar cell, which performs unassisted water splitting with a STH efficiency of up to 3.1%. The design relies on carefully selected redox mediators for the dye-sensitized solar cell as well as on surface passivation techniques and catalysts for the oxide-based photoanode (Figure 20).[90]

Another approach for harvesting visible light photons is through the design of new functional materials. Ng et al. transformed anodized tungsten oxide films ($WO_3 \cdot 2H_2O$) into bismuth tungstate (Bi_2WO_6) by substituting the intercalated water molecules with $[Bi_2O_2]^{2+}$ through a hydrothermal treatment (Figure 21).[93]

The resulting Bi_2WO_6 was readily used as an electrode to produce anodic photocurrents for H_2 evolution at the Pt counter electrode under visible light irradiation.[93] The degree of

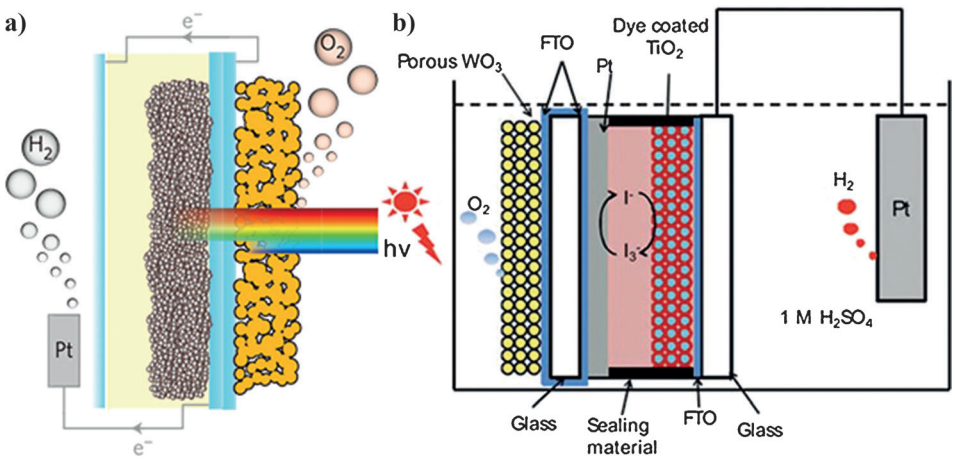

Figure 20. General schemes and energy diagrams for a photoanode/DSC D4 tandem cell: a) WO_3 tandem cell and b) dye coated TiO_2 porous WO_3 tandem cell. Red dotted lines indicate the reduction and oxidation potentials of water. Reprinted from Refs. [91] and [92].

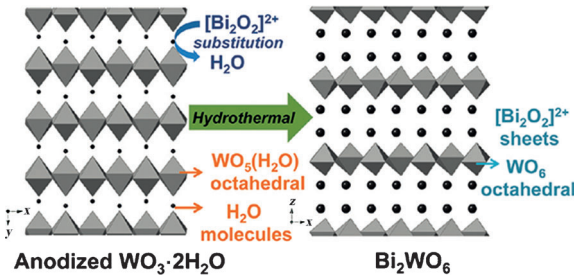

Figure 21. Structural transformation of anodized $WO_3 \cdot 2H_2O$ into Bi_2WO_6. Reprinted from Ref. [93].

light harvesting can be determined by the different opals WO_3 used. For example, Chen et al. demonstrated that photonic crystals could be used to improve light harvesting and photon-to-electron conversion efficiency at specific wavelengths by utilization of the slow-light effect in the inverse opals WO_3.[94] The spectral range at which the photon-to-electron conversion efficiency is enhanced is shifted to shorter wavelengths as the incident angle increases, which results from a blue shift in the stop-band center.

These findings suggest that the implementation of semiconducting photovoltaic devices in the form of photonic crystals to manipulate the behavior of photons and electrons is a feasible and effective way for enhancing the photon-to-electron conversion efficiency. It will also provide useful information for developing other visible-light-sensitive photoanodes with a photonic crystal structure. The increase of light absorption induced by the slow-light effect in the WO_3-200 inverse opal can be extended to the onset of visible region, as shown in Figure 22.[94]

As for the elucidation of charge-transfer processes in nanostructured WO_3, the recent developments are mainly based on the synthesis of multilayer thin films such as TiO_2/WO_3/Pt,[86] Ag/AgCl/plate-WO_3,[95] Mo-$BiVO_4/WO_3$,[87] $WO_3/Fe_2O_3/WO_3$, and $Fe_2O_3/WO_3/Fe_2O_3$.[8a] To achieve more effective PEC-driven water splitting, a hybrid photoelectrode based on PEC tandem cell design was developed.[91] Figures 23 and 24 show the summary of photoelectrochemical tandem cells for different photocatalysts. In addition, heterojunction structures can also offer

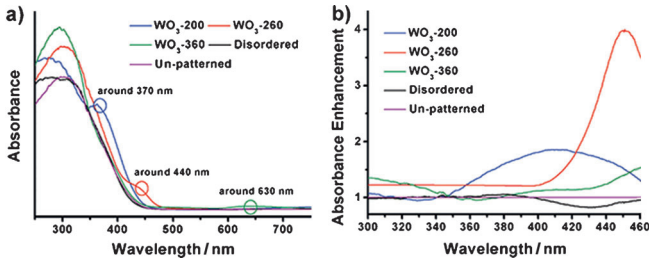

Figure 22. a) Light absorption spectra of WO_3 inverse opals, a disordered porous WO_3, and an unpatterned WO_3 photoanode measured at a normal incidence of light. The colored hollow circles show the slow light absorption at the red edge of the stop band for each inverse opal structure. b) Absorbance enhancement spectra (ratio of the absorbance of WO_3 inverse opals and disordered porous sample to that of the unpatterned WO_3 photoanode) as a function of the wavelength. Reprinted from Ref. [94].

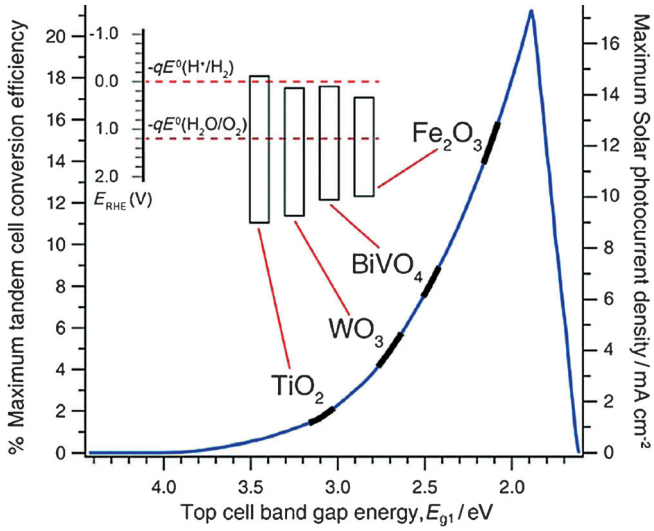

Figure 23. Maximum solar-to-hydrogen conversion efficiency and solar photocurrent as a function of the top cell band gap energy in a tandem cell. The band gap energies and efficiency range for commonly used semiconductor oxide photoanodes are also shown. Reprinted from Ref. [96].

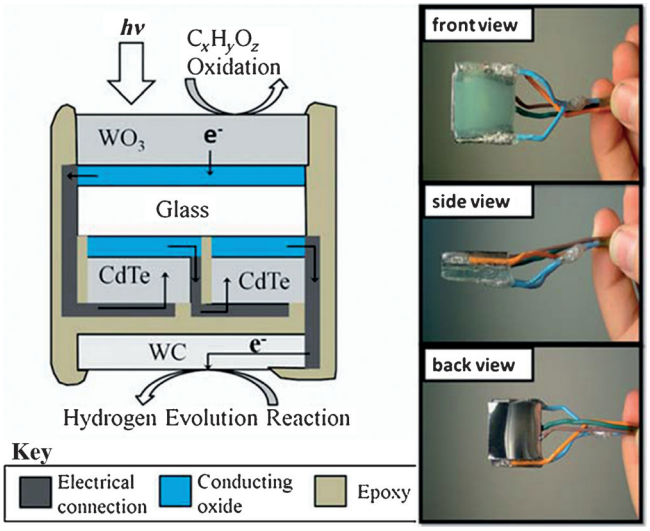

Figure 24. Schematic side view of a WO_3 | CdTe | WC tandem cell device and photographs of an actual device. External wires attached to each tandem cell component (WO_3, CdTe, WC) allow for measurement of the current–voltage characteristics of either the whole device or an individual component. Reprinted from Ref. [91].

enhanced separation of photogenerated charge carriers as previously reported for $WO_3/BiVO_4$,[67] Bi_2S_3/WO_3,[89] graphene oxide-WO_3,[88] and multiple (WO_3-Pt)/TiO_2.[89] The conduction band of WO_3 is not high enough to induce H^+ reduction. The enhanced electric field produced from the photoexcitation of a localized surface plasmon resonance (LSPR) peak of Au particles has been shown to improve the photocatalytic activity as evidenced by an increase in accompanying H_2 production. The optimal distance between Au and the semiconductor core, that is, CdS, remains an important factor in achieving a plasmon-induced enhancement of the PEC process. Transition

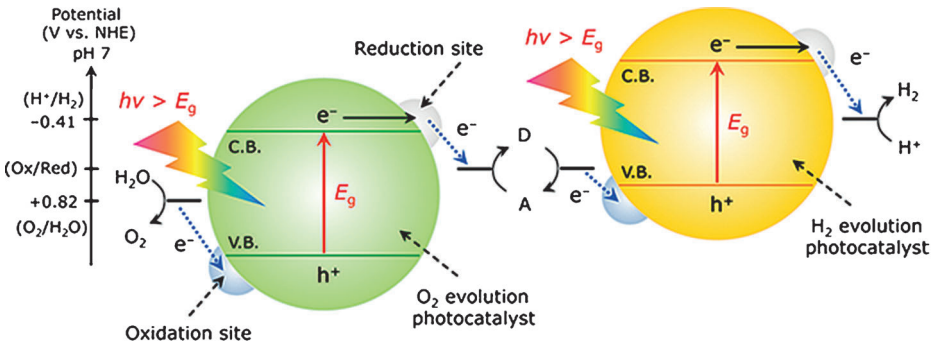

Figure 25. Energy diagram of photocatalytic water splitting for a two-step photoexcitation system (C.B. = conduction band, V.B. = valence band, E_g = band gap = . D and A indicate electron-donating and electron-accepting species, respectively. Reprinted from Ref. [98].

metal oxide nanocrystals are potential candidates as LSPR hosts because they exhibit interesting properties arising from the unique characteristic of their outer-d valence electrons. Manthiram and Alivisatos[97] demonstrated that the metallic phases of WO_3-δ nanoparticles exhibit a strong and tunable LSPR, which open up the possibility of designing plasmonic tungsten oxide nanoparticles with improved PEC activity.

In parallel, theoretical efforts have also been increasingly used to evaluate the energetics and predict the water-splitting efficiency of different semiconductor systems. In particular, DFT studies are useful for identifying the properties of doped semiconductors as well as for the design of new semiconductor photocatalysts. Theoretical and experimental efforts are currently leading the way in designing co-doped nanostructures semiconductor photocatalysts.

Lastly, the Z-Scheme is increasingly used for the conventional one-step water splitting systems as visible light and energy can be used more efficiently for improved H_2 production on semiconductor surfaces. Using the Z-scheme, it is possible to apply semiconductor photocatalyst films as photoelectrodes for either water reduction or oxidation. For example, WO_3 does not have the ability to reduce H^+, but is capable of producing O_2 from an aqueous solution containing appropriate electron acceptors under visible light. Thus, WO_3 can act as an effective building block for O_2 evolution in Z-Scheme water splitting. Similarly, other semiconductor photocatalysts capable of H^+ reduction can be utilized accordingly. Because both particles absorb light in the Z-scheme, it opens up new opportunities to modulate the two-photon process and, thus, overcome many of the energetic barriers for the design of hybrid assemblies that can utilize reduction and oxidation processes. The diagram of the Z-Scheme is shown in Figure 25. Wang et al. investigated the Si:WO_3 heterostructure for Z-Scheme water splitting.[8a] They found that a band alignment exists between Si and WO_3 with a 0.4–0.5 eV gap between the Si valence and WO_3 conduction band edges, which results in a small Schottky barrier between p-type Si and n-type WO_3. This finding can effectively improve the performance of photoelectrodes for Z-Scheme water splitting applications.

To date, various materials have been investigated as efficient photocathodes for H_2 generation such as p-Si, p-WO_3/Cu_2O with ZnO/Al and TiO_2, p-GO (p-type graphene oxide), and CdS-coated p-$CuGeSe_2$.[87,90] In these studies, the highest photocurrent density for photocathodes of over 10 mA cm^{-2} versus RHE potential has been reported. A recent study reported that the utilization of Ni/n-Si photoanode can achieve an even higher photocurrent density of 65 mA cm^{-2} at 1.2 V (vs. RHE).[94] However, the nominal range of photocurrent density reported for bare nanostructured WO_3 only ranged from 0.08 to 4 mA cm^{-2}.[8] Thus, the on-going challenge in synthesizing nanostructured WO_3 is to design WO_3-based nanostructures with high energy conversion efficiencies that could effectively utilize the solar spectrum to generate H_2 through water splitting.

7. Summary and Outlook

We critically reviewed nanostructured WO_3 synthesized through the electrochemical route for the application for photoelectrochemical (PEC) water splitting. The key fundamental reaction mechanisms as well as the various effects of synthesis methods and approaches on the eventual physical, chemical, optical, and photoelectrochemical properties of nanostructured WO_3 are explained in detail. Furthermore, we also raised the concern among the scientific community in the field with regard to standardization of the determination of the energy conversion efficiency for nanostructured WO_3 synthesized through different methods and approaches. Lastly, a summary of the current evaluation practices on the energy conversion efficiency of nanostructured WO_3 is given and further a recommendation is provided to standardize the research outcomes on PEC efficiencies for ease of comparison. Although nanostructured WO_3 has been widely synthesized, the PEC water splitting efficiency is still relatively low. This has remained as an on-going challenge in nanomaterials synthesis perspective in an attempt to improve the PEC water splitting and other energy conversion efficiencies in the near future.

Acknowledgements

The authors are grateful to the financial support provided by the eScience fund (Project No: 03-02-10-SF0121) from Ministry of Science, Technology and Innovation (MOSTI), Malaysia. Similar gratitude also goes to the Advanced Engineering Platform and School of Engineering, Monash University Malaysia.

Keywords: cathodes · electrodeposition · photocatalysis · water splitting · thin films

[1] J. R. Bartels, M. B. Pate, N. K. Olson, *Int. J. Hydrogen Energy* **2010**, *35*, 8371 – 8384.
[2] A. Fujishima, K. Honda, *Nature* **1972**, *238*, 37.
[3] a) S. Balachandran, M. Swaminathan, *J. Phys. Chem. C* **2012**, *116*, 26306 – 26312; b) S. Chen, W. Zhao, W. Liu, S. Zhang, *Appl. Surf. Sci.* **2008**, *255*, 2478 – 2484; c) H. Qin, W. Li, Y. Xia, T. He, *ACS Appl. Mater. Interfaces* **2011**, *3*, 3152 – 3156.
[4] a) Q. Han, Z. H. Liu, Y. Y. Xu, Z. Y. Chen, T. M. Wang, H. Zhang, *J. Phys. Chem. C* **2007**, *111*, 5034 – 5038; b) M. Niu, F. Huang, L. Cui, P. Huang, Y. Yu, Y. Wang, *ACS Nano* **2010**, *4*, 681 – 688; c) Y. Shi, H. Li, L. Wang, W. Shen, H. Chen, *ACS Appl. Mater. Interfaces* **2012**, *4*, 4800 – 4806.
[5] a) F. Magalhães, F. C. C. Moura, R. M. Lago, *Desalination* **2011**, *276*, 266 – 271; b) C. Shifu, Z. Sujuan, L. Wei, Z. Wei, *J. Hazard. Mater.* **2008**, *155*, 320 – 326; c) V. Vimonses, M. N. Chong, B. Jin, *Microporous Mesoporous Mater.* **2010**, *132*, 201 – 209.
[6] H. Ishihara, G. K. Kannarpady, K. R. Khedir, J. Woo, S. Trigwell, A. S. Biris, *Phys. Chem. Chem. Phys.* **2011**, *13*, 19553 – 19560.
[7] K.-S. Ahn, S.-H. Lee, A. C. Dillon, C. E. Tracy, R. Pitts, *J. Appl. Phys.* **2007**, *101*, 093524.
[8] a) S. S. Kalanur, Y. J. Hwang, S. Y. Chae, O. S. Joo, *J. Mater. Chem. A* **2013**, *1*, 3479 – 3488; b) V. S. Vidyarthi, M. Hofmann, A. Savan, K. Sliozberg, D. König, R. Beranek, W. Schuhmann, A. Ludwig, *Int. J. Hydrogen Energy* **2011**, *36*, 4724 – 4731; c) X. M. Zhang, K. Huo, L. Hu, P. K. Chu, *IEEE Nanoelectronics Conference* **2010**, 1090 – 1091; d) S. Yousefzadeh, A. Reyhani, N. Naseri, A. Z. Moshfegh, *J. Solid State Chem.* **2013**, *204*, 341 – 347.
[9] a) C. Cantalini, W. Wlodarski, Y. Li, M. Passacantando, S. Santucci, E. Comini, G. Faglia, G. Sberveglieri, *Sens. Actuators B* **2000**, *64*, 182 – 188; b) W. Li, C. Liu, Y. Yang, J. Li, Q. Chen, F. Liu, *Mater. Lett.* **2012**, *84*, 41 – 43; c) H. Zheng, A. Z. Sadek, K. Latham, K. Kalantar-Zadeh, *Electrochem. Commun.* **2009**, *11*, 768 – 771.
[10] a) Q. Mi, Y. Ping, Y. Li, B. Cao, B. S. Brunschwig, P. G. Khalifah, G. A. Galli, H. B. Gray, N. S. Lewis, *J. Am. Chem. Soc.* **2012**, *134*, 18318 – 18324; b) K. J. Patel, C. J. Panchal, M. S. Desai, P. K. Mehta, *Mater. Chem. Phys.* **2010**, *124*, 884 – 890; c) A. Ponzoni, E. Comini, M. Ferroni, G. Sberveglieri, *Thin Solid Films* **2005**, *490*, 81 – 85.
[11] a) D. Gogova, G. Stoyanov, K. A. Gesheva, *Renewable Energy* **1996**, *8*, 546 – 550; b) J. Goschnick, M. Frietsch, T. Schneider, *Surface and Coatings Technology* **1998**, *108 – 109*, 292 – 296; c) Z. S. Houweling, J. W. Geus, R. E. I. Schropp, *Mater. Chem. Phys.* **2013**, *140*, 89 – 96.
[12] a) W. L. Kwong, N. Savvides, C. C. Sorrell, *Electrochim. Acta* **2012**, *75*, 371 – 380; b) T. Pauporté, A. Goux, A. Kahn-Harari, N. de Tacconi, C. R. Chenthamarakshan, K. Rajeshwar, D. Lincot, *J. Phys. Chem. Solids* **2003**, *64*, 1737 – 1742; c) I. Zhitomirsky, *Adv. Colloid Interface Sci.* **2002**, *97*, 279 – 317.
[13] a) C. A. Bignozzi, S. Caramori, V. Cristino, R. Argazzi, L. Meda, A. Tacca, *Chem. Soc. Rev.* **2013**, *42*, 2228 – 2246; b) V. Cristino, S. Caramori, R. Argazzi, L. Meda, G. L. Marra, C. A. Bignozzi, *Langmuir* **2011**, *27*, 7276 – 7284; c) A. Watcharenwong, W. Chanmanee, N. R. de Tacconi, C. R. Chenthamarakshan, P. Kajitvichyanukul, K. Rajeshwar, *J. Electroanal. Chem.* **2008**, *612*, 112 – 120.
[14] a) K.-I. Liu, Y.-C. Hsueh, C.-Y. Su, T.-P. Perng, *Int. J. Hydrogen Energy* **2013**, *38*, 7750 – 7755; b) N. Naseri, S. Yousefzadeh, E. Daryaei, A. Z. Moshfegh, *Int. J. Hydrogen Energy* **2011**, *36*, 13461 – 13472.
[15] M.-S. Gui, W.-D. Zhang, Y.-Q. Chang, Y.-X. Yu, *Chem. Eng. J.* **2012**, *197*, 283 – 288.
[16] S. Wei, Y. Ma, Y. Chen, L. Liu, Y. Liu, Z. Shao, *J. Hazard. Mater.* **2011**, *194*, 243 – 249.
[17] R. Vijayalakshmi, *Synth. React. Inorg. Metal-Org. Nano-Metal Chem.* **2006**, *36*, 89 – 94.
[18] a) N. Sonoyama, K. Iwase, H. Takatsuka, T. Matsumura, N. Imanishi, Y. Takeda, R. Kanno, *J. Power Sources* **2009**, *189*, 561 – 565; b) M. Plaza, M. Abuín, A. Mascaraque, M. A. González-Barrio, L. Pérez, *Mater. Chem. Phys.* **2012**, *134*, 523 – 530.
[19] a) P. E. Hovsepian, D. B. Lewis, Q. Luo, A. Farinotti, *Thin Solid Films* **2005**, *488*, 1 – 8; b) R. Vaidyanathan, S. M. Cox, U. Happek, D. Banga, M. K. Mathe, J. L. Stickney, *Langmuir* **2006**, *22*, 10590 – 10595.
[20] a) S. Feng, J. Yang, M. Liu, H. Zhu, J. Zhang, G. Li, J. Peng, Q. Liu, *Electrochim. Acta* **2012**, *83*, 321 – 326; b) S. Li, H. Zhao, D. Tian, *Mater. Sci. Semicond. Proc.* **2013**, *16*, 149 – 153.
[21] a) D. J. Comstock, S. T. Christensen, J. W. Elam, M. J. Pellin, M. C. Hersam, *Electrochem. Commun.* **2010**, *12*, 1543 – 1546; b) S. Bai, C. Sun, T. Guo, R. Luo, Y. Lin, A. Chen, L. Sun, J. Zhang, *Electrochim. Acta* **2013**, *90*, 530 – 534; c) K. Liang, X. Tang, B. Wei, W. Hu, *Mater. Res. Bull.* **2013**, *48*, 3829 – 3833.
[22] a) S. Gupta, M. Tripathi, S. Gupta, M. Tripathi, M. Tripathi, *Centr. Eur. J. Chem.* **2011**, *10*, 279 – 294; b) S. Kim, J. Choi, S. Kim, J. Choi, *Electrochem. Commun.* **2012**, *17*, 10 – 13.
[23] L. E. Fraga, M. V. B. Zanoni, L. E. Fraga, M. V. B. Zanoni, *J. Braz. Chem. Soc.* **2011**, *22*, 718 – 725.
[24] R. Hahn, J. M. Macak, P. Schmuki, *Electrochem. Commun.* **2007**, *9*, 947 – 952.
[25] N. Mukherjee, M. Paulose, O. K. Varghese, G. K. Mor, C. A. Grimes, N. Mukherjee, M. Paulose, O. K. Varghese, G. K. Mor, C. A. Grimes, *J. Mater. Res.* **2003**, *18*, 2296 – 2299.
[26] Y.-c. Nah, I. Paramasivam, R. Hahn, N. K. Shrestha, P. Schmuki, *Nanotechnology* **2010**, *21*, 105704.
[27] Y. Liu, Y. Li, W. Li, S. Han, C. Liu, *Appl. Surf. Sci.* **2012**, *258*, 5038 – 5045.
[28] H. Tsuchiya, J. M. Macak, I. Sieber, L. Taveira, A. Ghicov, K. Sirotna, P. Schmuki, *Electrochem. Commun.* **2005**, *7*, 295 – 298.
[29] B. Yang, H. Li, M. Blackford, V. Luca, *Curr. Appl. Phys.* **2006**, *6*, 436 – 439.
[30] E. A. Meulenkamp, *J. Electrochem. Soc.* **1997**, *144*, 1664.
[31] P. K. Shen, A. C. C. Tseung, *J. Mater. Chem.* **1992**, *2*, 1141 – 1147.
[32] B.-X. Zou, Y. Liang, X.-X. Liu, D. Diamond, K.-T. Lau, *J. Power Sources* **2011**, *196*, 4842 – 4848.
[33] G. Leftheriotis, P. Yianoulis, *Solid State Ionics* **2008**, *179*, 2192 – 2197.
[34] N. R. de Tacconi, C. R. Chenthamarakshan, K. Rajeshwar, T. Pauporté, D. Lincot, *Electrochem. Commun.* **2003**, *5*, 220 – 224.
[35] M. Yagi, K. Sone, M. Yamada, S. Umemiya, *Chem. Eur. J.* **2005**, *11*, 767 – 775.
[36] Q. Zhao, Z. Yu, W. Yuan, J. Li, *Int. J. Hydrogen Energy* **2012**, *37*, 13249 – 13255.
[37] P. M. S. Monk, S. L. Chester, *Electrochim. Acta* **1993**, *38*, 1521 – 1526.
[38] Z. Yu, X. Jia, J. Du, J. Zhang, *Solar Ener. Mater. Solar Cells* **2000**, *64*, 55 – 63.
[39] R. Vijayalakshmi, M. Jayachandran, C. Sanjeeviraja, *Curr. Appl. Phys.* **2003**, *3*, 171 – 175.
[40] T. Pauporte, *J. Electrochem. Soc.* **2002**, *149*, C539 – C545.
[41] A. J. Martín, A. M. Chaparro, L. Daza, *J. Power Sources* **2011**, *196*, 4187 – 4192.
[42] S. H. Baeck, K. S. Choi, T. F. Jaramillo, G. D. Stucky, E. W. McFarland, *Adv. Mater.* **2003**, *15*, 1269 – 1273.
[43] W. L. Kwong, A. Nakaruk, P. Koshy, C. C. Sorrell, *Thin Solid Films* **2013**, *544*, 191 – 196.
[44] J.-J. Feng, J.-J. Xu, H.-Y. Chen, *Electrochem. Commun.* **2006**, *8*, 77 – 82.
[45] H. Y. Yin, X. C. Song, Y. F. Zheng, X. Wang, Z. A. Yang, R. Ma, *Mater. Sci. Eng. B* **2011**, *176*, 684 – 687.
[46] J. C. Hill, K.-S. Choi, *J. Phys. Chem. C* **2012**, *116*, 7612 – 7620.
[47] W. Zhao, Z. Wang, X. Shen, J. Li, C. Xu, Z. Gan, *Int. J. Hydrogen Energy* **2012**, *37*, 908 – 915.
[48] S. Somasundaram, C. R. Chenthamarakshan, N. R. de Tacconi, N. A. Basit, K. Rajeshwar, *Electrochem. Commun.* **2006**, *8*, 539 – 543.
[49] S. H. Baeck, T. Jaramillo, G. D. Stucky, E. W. McFarland, *Nano Lett.* **2002**, *2*, 831 – 834.
[50] L. Kondrachova, B. P. Hahn, G. Vijayaraghavan, R. D. Williams, K. J. Stevenson, L. Kondrachova, B. P. Hahn, G. Vijayaraghavan, R. D. Williams, K. J. Stevenson, *Langmuir* **2006**, *22*, 10490.
[51] M. C. Martínez-Rivera, B. W. Berry, K. G. Valentine, K. Westerlund, S. Hay, C. Tommos, *J. Am. Chem. Soc.* **2011**, *133*, 17786 – 17795.
[52] A. Di Paola, F. Di Quarto, C. Sunseri, *Corros. Sci.* **1980**, *20*, 1067 – 1078.
[53] E. Patrick, M. E. Orazem, J. C. Sanchez, T. Nishida, *J. Neurosci. Methods* **2011**, *198*, 158 – 171.
[54] Z. a. Chen, *PEC EXPERIMENT STANDARD*, Springer, Berlin/New York, **2013**.
[55] S. Berger, H. Tsuchiya, A. Ghicov, P. Schmuki, *Appl. Phys. Lett.* **2006**, *88*, 203119.
[56] Y.-C. Nah, A. Ghicov, D. Kim, P. Schmuki, *Electrochem. Commun.* **2008**, *10*, 1777 – 1780.
[57] N. Li, B. Zhou, P. Guo, J. Zhou, D. Jing, *Int. J. Hydrogen Energy* **2013**, *38*, 11268 – 11277.
[58] D. Huang, L. Wang, Q. Xue, *Solid State Sci.* **2011**, *13*, 653 – 657.
[59] W. J. Lee, P. S. Shinde, G. H. Go, C. H. Doh, *Appl. Surf. Sci.* **2013**, *270*, 267 – 271.

[60] M. Seifollahi Bazarjani, M. Hojamberdiev, K. Morita, G. Zhu, G. Cherkashinin, C. Fasel, T. Herrmann, H. Breitzke, A. Gurlo, R. Riedel, *J. Am. Chem. Soc.* **2013**, *135*, 4467 – 4475.
[61] C. Ng, Y. H. Ng, A. Iwase, R. Amal, *ACS Appl. Mater. Interfaces* **2013**, *5*, 5269 – 5275.
[62] S. J. Hong, H. Jun, P. H. Borse, J. S. Lee, *Int. J. Hydrogen Energy* **2009**, *34*, 3234 – 3242.
[63] X. Liu, F. Wang, Q. Wang, X. Liu, F. Wang, Q. Wang, *Phys. Chem. Chem. Phys.* **2012**, *14*, 7894 – 7911.
[64] M. Regragui, M. Addou, B. El Idrissi, J. C. Bernède, A. Outzourhit, E. Ecchamikh, *Mater. Chem. Phys.* **2001**, *70*, 84 – 89.
[65] H. Tong, S. Ouyang, Y. Bi, N. Umezawa, M. Oshikiri, J. Ye, *Adv. Mater.* **2012**, *24*, 229 – 251.
[66] R. Saito, Y. Miseki, K. Sayama, *Chem. Commun.* **2012**, *48*, 3833 – 3835.
[67] C. W. Lai, S. Sreekantan, *Electrochim. Acta* **2013**, *87*, 294 – 302.
[68] K. C. Leonard, K. M. Nam, H. C. Lee, S. H. Kang, H. S. Park, A. J. Bard, *J. Phys. Chem. C* **2013**, *117*, 15901 – 15910.
[69] M. Yagi, S. Umemiya, *J. Phys. Chem. B* **2002**, *106*, 6355 – 6357.
[70] G. Wang, Y. Ling, H. Wang, X. Yang, C. Wang, J. Z. Zhang, Y. Li, *Energy Environ. Sci.* **2012**, *5*, 6180 – 6187.
[71] W. Zhao, Y. Yang, H. Zhang, *Electrochim. Acta* **2013**, *99*, 273 – 277.
[72] G. Liu, P. Niu, H. M. Cheng, *ChemPhysChem* **2013**, *14*, 885 – 892.
[73] F. Amano, E. Ishinaga, A. Yamakata, *J. Phys. Chem. C* **2013**, *117*, 22584 – 22590.
[74] M.-R. Gao, Y.-F. Xu, J. Jiang, S.-H. Yu, *Chem. Soc. Rev.* **2013**, *42*, 2986 – 3017.
[75] G.-R. Li, H. Xu, X.-F. Lu, J.-X. Feng, Y.-X. Tong, C.-Y. Su, *Nanoscale* **2013**, *5*, 4056 – 4069.
[76] G. Xi, J. Ye, Q. Ma, N. Su, H. Bai, C. Wang, *J. Am. Chem. Soc.* **2012**, *134*, 6508 – 6511.
[77] F. Riboni, L. G. Bettini, D. W. Bahnemann, E. Selli, *Catal. Today* **2013**, *209*, 28 – 34.
[78] S. S. K. Ma, K. Maeda, R. Abe, K. Domen, *Energy Environ. Sci.* **2012**, *5*, 8390 – 8397.
[79] D. Barreca, G. Carraro, V. Gombac, A. Gasparotto, C. Maccato, P. Fornasiero, E. Tondello, *Adv. Funct. Mater.* **2011**, *21*, 2611 – 2623.
[80] T. K. Townsend, N. D. Browning, F. E. Osterloh, *Energy Environ. Sci.* **2012**, *5*, 9543 – 9550.
[81] D. V. Esposito, I. Levin, T. P. Moffat, A. A. Talin, *Nat. Mater.* **2013**, *12*, 562 – 628.
[82] J. Sun, D. K. Zhong, D. R. Gamelin, *Energy Environ. Sci.* **2010**, *3*, 1252 – 1261.
[83] M. Yoshida, A. Yamakata, K. Takanabe, J. Kubota, M. Osawa, K. Domen, *J. Am. Chem. Soc.* **2009**, *131*, 13218 – 13219.
[84] A. Tanaka, K. Fuku, T. Nishi, K. Hashimoto, H. Kominami, *J. Phys. Chem. C* **2013**, *117*, 16983 – 16989.
[85] W. Fan, Q. Zhang, Y. Wang, *Phys. Chem. Chem. Phys.* **2013**, *15*, 2632 – 2649.
[86] Z. Mou, S. Yin, M. Zhu, Y. Du, X. Wang, P. Yang, J. Zheng, C. Lu, *Phys. Chem. Chem. Phys.* **2013**, *15*, 2793 – 2799.
[87] Y. Qu, X. Duan, *Chem. Soc. Rev.* **2013**, *42*, 2568 – 2580.
[88] S. Ahmed, I. A. I. Hassan, H. Roy, F. Marken, *J. Phys. Chem. C* **2013**, *117*, 7005 – 7012.
[89] R. Solarska, R. Jurczakowski, J. Augustynski, *Nanoscale* **2012**, *4*, 1553 – 1556.
[90] J. Brillet, J.-h. Yum, M. Cornuz, T. Hisatomi, R. Solarska, J. Augustynski, M. Grätzel, K. Sivula, *Nat. Photonics* **2012**, *6*, 824.
[91] D. V. Esposito, R. V. Forest, Y. Chang, N. Gaillard, B. E. McCandless, S. Hou, K. H. Lee, R. W. Birkmire, J. G. Chen, *Energy Environ. Sci.* **2012**, *5*, 9091 – 9099.
[92] J. K. Kim, K. Shin, S. M. Cho, T.-W. Lee, J. H. Park, *Energy Environ. Sci.* **2011**, *4*, 1465 – 1470.
[93] C. Ng, A. Iwase, Y. H. Ng, R. Amal, *J. Phys. Chem. Lett.* **2012**, *3*, 913 – 918.
[94] X. Chen, J. Ye, S. Ouyang, T. Kako, Z. Li, Z. Zou, *ACS Nano* **2011**, *5*, 4310 – 4318.
[95] D. Chen, T. Li, Q. Chen, J. Gao, B. Fan, J. Li, X. Li, R. Zhang, J. Sun, L. Gao, *Nanoscale* **2012**, *4*, 5431 – 5439.
[96] M. S. Prévot, K. Sivula, *J. Phys. Chem. C* **2013**, *117*, 17879 – 17893.
[97] K. Manthiram, A. P. Alivisatos, *J. Am. Chem. Soc.* **2012**, *134*, 3995 – 3998.
[98] K. Maeda, *ACS Catal.* **2013**, *3*, 1486 – 1503.

Received: February 21, 2014
Revised: May 30, 2014
Published online on October 2, 2014